

Trends and drivers of ecosystem water use efficiency and carbon uptake modeled across South Asia

Arijit Chakraborty^{a,1} , Manabendra Saharia^{a,b,*} , Sumedha Chakma^a, Sujay V. Kumar^c

^a Department of Civil Engineering, Indian Institute of Technology Delhi, Hauz Khas, New Delhi 110016, India

^b Yardi School of Artificial Intelligence, Indian Institute of Technology Delhi, Hauz Khas, New Delhi 110016, India

^c Hydrological Sciences Laboratory, NASA Goddard Space Flight Center, Greenbelt, MD, United States

ARTICLE INFO

Keywords:

Water use efficiency
Dynamic vegetation scheme
Land surface model
ILDAS
Sensitivity analysis

ABSTRACT

Quantifying the influence of vegetation dynamics on carbon uptake and its climatic drivers is critical for regional carbon-cycle assessments, yet most land surface modeling studies still parameterize static vegetation. This limitation is particularly relevant in South Asia, where widespread vegetation greening has altered ecosystem productivity. This study focuses on the spatiotemporal variability of gross primary productivity (GPP), evapotranspiration (ET), and the resulting ecosystem water-use efficiency ($WUE = GPP/ET$) to understand the long-term trends and drivers across South Asia. Simulations are performed over South Asia for 1985–2023 using the Indian Land Data Assimilation System (ILDAS) with a dynamic vegetation scheme and hybrid meteorological forcing involving local IMD (India Meteorological Department) precipitation while maintaining transboundary consistency. Results reveal significant regional variations with high GPP ($>2500 \text{ g.C/m}^2/\text{year}$) and WUE ($> 2 \text{ g.C/kg H}_2\text{O/year}$) over the lower Himalayan and northeastern regions, and low values over arid north-western region. Seasonal variability peaks during the monsoon for GPP ($\sigma = 95.44 \text{ g C/m}^2$) and ET ($\sigma = 39.60 \text{ mm}$), whereas WUE varies the most in the pre-monsoon ($\sigma = 12.48 \text{ g C/m}^2/\text{mm}$), reflecting vegetation adaptation under water-limited conditions. Non-parametric elasticity analysis indicates temperature ($\epsilon = -21.78$) and pressure ($\epsilon = 76.30$) as dominant climatic drivers of WUE, while soil moisture and leaf area index (LAI) are the primary internal drivers. Trend analysis reveals significant increases ($p < 0.05$) in GPP and WUE across large parts of South Asia, particularly in northern and central agro-ecological zones, consistent with vegetation greening within existing forest cover. Model evaluation shows stronger agreement for GPP with FluxSat (median $R = 0.70$; KGE = 0.43) than with MODIS, and robust ET performance against MODIS (median $R = 0.81$; KGE = 0.44) over vegetated regions. In the absence of direct observations, cross-validation of modeled WUE with MODIS-derived WUE indicates moderate agreement (median $R = 0.36$) but low KGE (0.21), reflecting uncertainties in ratio-based diagnostics. Overall, the spatial coherence of errors supports the utility of the current ILDAS framework with dynamic vegetation scheme for assessing long-term carbon–water interactions across South Asia.

1. Introduction

Gross primary production (GPP) refers to the total amount of carbon that vegetation takes in at the ecosystem level. It is the main factor in the land carbon budget and has a significant impact on global carbon sequestration (Anav et al., 2015; Chapin et al., 2006). The absorption of carbon by ecosystems is mostly controlled by photosynthesis, a plant physiological process that is significantly influenced by climatic, hydrological, and biological factors (Zscheischler et al., 2017). Therefore,

GPP serves as a measure of the effectiveness of ecosystems and the efficiency of carbon flux resulting from eco-physiological processes (Collalti and Prentice, 2019). Measuring the spatial and temporal variations of Gross Primary Productivity (GPP) is crucial for gaining a better understanding of the Earth's terrestrial ecosystems and how they influence climate change (Campbell et al., 2017; Uchale et al., 2023). However, representation of such plant-physiological processes and their influence on water and carbon cycle is sparse in land surface process modeling. Evapotranspiration (ET) is considered a significant climatic

* Corresponding author at: Department of Civil Engineering, Indian Institute of Technology Delhi, Hauz Khas, New Delhi 110016, India.

E-mail address: msaharia@iitd.ac.in (M. Saharia).

¹ Current Affiliation: Department of Civil Engineering, Division of Hydraulics and Geotechnics, KU Leuven, 3001 Leuven, Heverlee, Belgium

indicator that connects the carbon, water, and energy cycles to assess the condition of surface water (Allen et al., 2011; Kumar and Sharma, 2023; Qiu et al., 2025; Wang and Dickinson, 2012). Variations in ecological aridity can be quantified by observing alterations in ecosystem productivity and Water Use Efficiency (WUE) under changing climatic conditions (Greve et al., 2017; Roderick et al., 2015). Evaporation and the physical characteristics of vegetation play important roles in determining the WUE of an ecosystem (Tang et al., 2014). Thus, it is crucial to measure the spatiotemporal variability, as well as the changing trend, of GPP and WUE under different agro-ecological and land cover scenarios for the better understanding of the terrestrial ecosystem's response to climate change (Campbell et al., 2017; Huang et al., 2015; Huxman et al., 2004; Niu et al., 2011; Uchale et al., 2023). Moreover, sensitivity of WUE towards other land surface state variables is less explored over South Asia, which could have helped in identifying the most influential driving factors of WUE. In fact, very few studies have contrasted the variation of GPP and WUE based on different land covers over this region. Moreover, the dynamic simulation of carbon uptake by various canopy components into a model and its impact in estimating the carbon fluxes have not been investigated yet using the Indian Land Data Assimilation System (ILDAS), which is a transboundary hydrologic-hydrodynamic modelling system designed to estimate land surface conditions and water fluxes in South Asia (Chakraborty et al., 2024; Magotra et al., 2024a, 2024b). In the earlier versions of ILDAS, vegetation dynamics were modeled by using predefined LAI values with a lookup table (Ek et al., 2003), which limited the models' ability to describe the responses of vegetation to weather and climate change. The seasonal variation in vegetation growth stages influences their carbon uptake as well and hence it has become necessary to include these processes into land surface modeling studies for better understanding of the water and carbon usage by the terrestrial ecosystem.

WUE is the ratio of carbon assimilated to water lost in terms of evapotranspiration in terrestrial ecosystems (Baldocchi, 1994; Xue et al., 2021; Zhang et al., 2016), indicating the balance between carbon and water fluxes (Keenan et al., 2013a; Tang et al., 2014). It establishes link between the carbon and water balance (El Masri et al., 2019; Tang et al., 2014). In-situ estimates as well as modeling approaches have been extensively used to evaluate carbon fluxes. Ecosystem-level carbon and water exchanges can be continuously measured using the in-situ eddy covariance (EC) approach (Baldocchi et al., 2001). This method enables the precise quantification of the net carbon exchange between the terrestrial ecosystem and the atmosphere (Chapin et al., 2006) and then segregation into GPP and ecosystem respiration (Reichstein et al., 2005). Additionally, fluctuations in WUE modeled from those in-situ measurements and its relation with different environmental conditions have been evaluated across a range of time intervals (Keenan et al., 2013a; Tang et al., 2014; Xiao et al., 2013). But this method only provides site-level estimates, which limits its applicability in developing countries like India, due to less availability of in-situ data. Under such circumstances, satellite remote sensing has opened up a new avenue for observing ecosystem carbon dynamics at a larger extent (Frankenberg et al., 2011; Justice et al., 2002; Xia et al., 2015). Numerous studies have documented the temporal and spatial fluctuations in primary production and WUE at both the regional and global scales (Kumar and Sharma, 2023; Sarmah et al., 2021; Sharma and Goyal, 2018; Tang et al., 2014; Tesfaye et al., 2021). However, these remote sensing observations often exhibit limitations in algorithmic performance and other technical criteria (Kim et al., 2020; Li et al., 2018; Loew et al., 2013). Process-based ecosystem models and remote sensing methods have been utilized now a days for better understanding of carbon-water interactions and water use efficiency in various environments on a large scale (Ito and Inatomi, 2012; Tian et al., 2010; Zhang et al., 2014). In recent years, Land Surface Models (LSM) have been extensively employed to simulate complex land surface processes and estimate relevant state variables, such as water and carbon fluxes (Dai et al., 2003; Ek et al., 2003; Koster et al., 2000; Niu et al., 2011). The

integration of a dynamic vegetation scheme allows Land Surface Models (LSMs) to simulate carbon cycle and biochemical processes by taking into account of the distribution of carbon in different parts of plants, such as leaves, roots, and stems. This enables LSMs to provide a predictive representation of vegetation growth by considering canopy states, such as Leaf Area Index (LAI) (He et al., 2023; Hosseini et al., 2022; Mengoli et al., 2022). In fact, the recent study conducted by Uchale et al., (2023) highlighted the need for a dynamic vegetation scheme calibrated and validated especially for India.

Earlier studies have examined the impact of various controlling factors on ecosystem carbon uptake and water use efficiency (Cheng et al., 2017; Lin et al., 2018; Sarmah et al., 2021; Sun et al., 2021; Tang et al., 2016). Few of such studies have been conducted over India in recent past (Dubey and Ghosh, 2023; Nandy et al., 2022; Peddinti et al., 2020; Sharma and Goyal, 2018; Verma et al., 2022; Verma and Ghosh, 2024). The studies conducted based on satellite data products often lack in considering carbon fertilisation and capturing the carbon dynamics precisely (Das et al., 2023; Kashyap et al., 2023). But, the implementation of land surface modelling framework along with dynamic vegetation scheme for estimating water use efficiency is rarely explored over the Indian subcontinent (Uchale et al., 2023). Providing a better representation of vegetation dynamics in LSMs can enhance the accuracy of ET calculations in numerical weather prediction (Boussetta et al., 2013), or vegetation dynamics under climatic variability (Laanaia et al., 2016) and its influence on carbon cycle (Green et al., 2019). Indian subcontinent is a significant contributor to global greening (Chen et al., 2019). This region exhibits large variability in climatic conditions, land covers, phenological growth (Champion and Seth, 1968). Consequently, a huge diversity in ecosystem exists here which enables different carbon sequestration patterns over the domain. However, a large degree of uncertainty exists in their estimations because of the lack of an extensive ground-monitoring network outfitted with EC flux towers (Chakraborty et al., 2020; Deb Burman et al., 2017; Uchale et al., 2023). In this study, a dynamic vegetation scheme has been introduced to observe the model's applicability in observing the spatiotemporal variations in carbon flux estimates over the Indian subcontinent. In this study, we assess spatial and temporal dynamics of GPP and resulting impact on WUE of terrestrial ecosystems of South Asia for a 40-year period (1985–2023). The present study focuses on:

- To observe the spatiotemporal variation of model estimated GPP, ET and resulting WUE across different seasons and land covers within South Asia,
- To analyze long-term trends in GPP and WUE over the study period.
- To assess the impact of different forcings variables on model estimated WUE in terms of sensitivity analysis.

2. Materials and methods

2.1. Study area

This study focuses on the South Asian domain covering all the Indian national and transboundary river basins within the geographical coordinates of 64.5°E – 100.0°E and 5.0°N – 38.0°N, shown in Fig. 1. We expanded the geographical reach of our study outside India to enable the Land Surface Model (LSM) to analyze the impact of different meteorological and geological conditions on different land surface state variables at the Indian landmass border. The domain comprises 18 major river basins consisting of 3 transboundary river basins, along with variation in topography, land cover (Fig. 1) and climatic conditions leading to significant variation in rainfall patterns, soil type and vegetation. The domain contains large Himalayan Forest, savannas, grasslands and croplands, signifying the diversity in land cover and vegetation types here. Many research and surveys support the fact of increasing tree cover in India up to 24.5% (Chaudhry and Tambe, 2023; G et al., 2022), indicating increase in photosynthetic activities and their

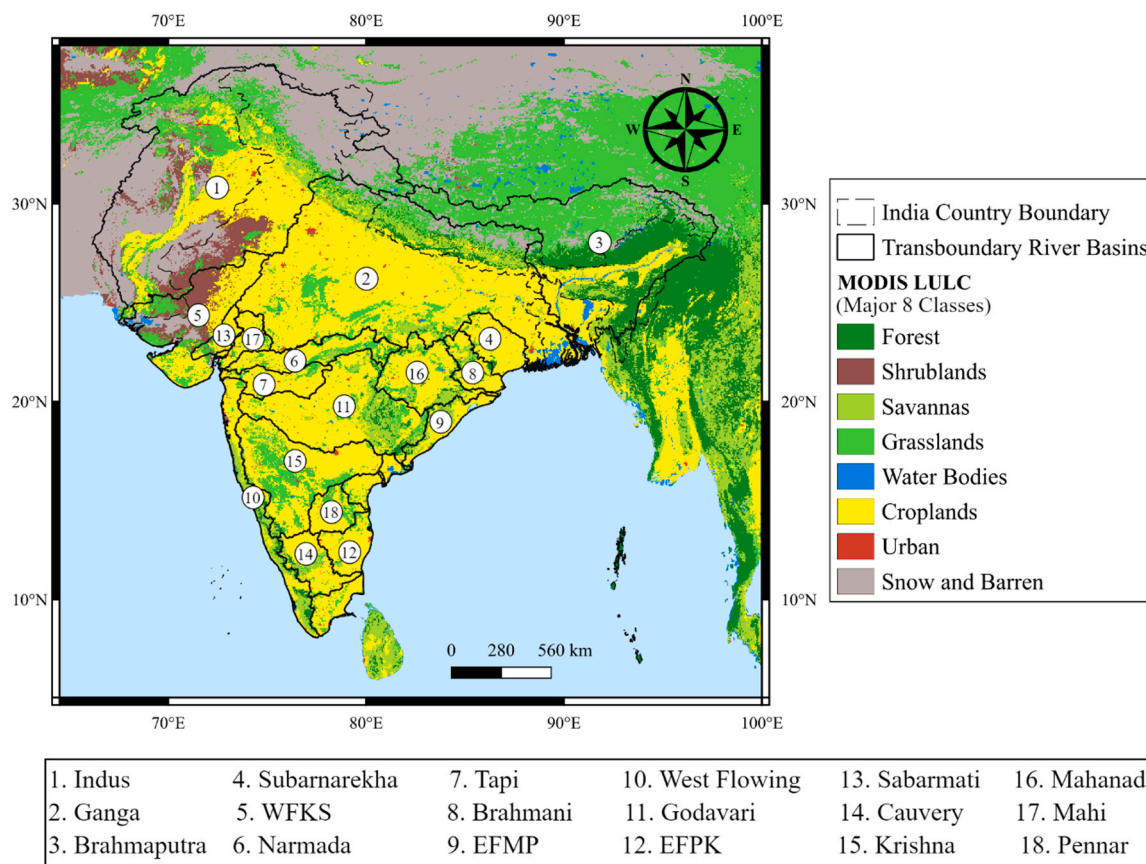


Fig. 1. Study Area covering the transboundary river basins of south Asia. All the basin names are shown in the box below the plot with their corresponding numbers. Abbreviations of Basin name are explained in the [Table S1](#) of [supplementary material](#).

impact on ecosystem water use efficiency.

Moreover, the role of precise consideration of vegetation dynamics is quite essential for various other hydrological and ecological applications over this highly diverse domain.

2.2. Meteorological forcings

2.2.1. India meteorological department (IMD) precipitation data

This research employed the India Meteorological Department (IMD) generated daily precipitation data at a 0.25° spatial resolution, spanning the years 1981–2022 ([Pai et al., 2014](#)) as precipitation input to the model. The dataset was generated using the inverse distance weighted (IDW) interpolation method, which was based on the data collected from a nationwide network of 6995 gauge stations ([Shepard, 1968](#)).

2.2.2. Modern-era retrospective analysis for research and applications (MERRA2)

The Modern-Era Retrospective Analysis for Research and Applications, Version 2 (MERRA-2; [Gelaro et al., 2017](#)) provides data beginning from 1980. It includes latest features from NASA's Global Modeling and Assimilation Office (GMAO). MERRA2 has demonstrated significant improvements over its previous product, MERRA ([Gelaro et al., 2017](#)). The study utilized the MERRA2 dataset corrected for biases, which features hourly time intervals and spatial resolution of 0.625° x 0.5°. The list of forcing variables and their sources is enlisted in [Table 1](#).

2.3. Evaluation datasets: gross primary productivity and evapotranspiration data

For evaluating the model results of GPP and ET we used the following satellite and machine learning model-derived global datasets:

Table 1

List of meteorological forcing variables used as input, their short name, units and their sources.

Forcing variable	Short name	Unit	Source
Precipitation	P	kg/m2	IMD
Near surface air temperature	T	K	
Specific Humidity	Q	kg/kg	
Shortwave radiation	SW	W/m2	MERRA2
Longwave radiation	LW	W/m2	
Windspeed	V	m/s	
Surface pressure	PS	Pa	

MODIS Gross Primary Productivity: We used the Terra MODIS gross primary productivity product MOD17A2H (Collection 6.1; [Running and Zhao, 2021](#)), which provides 8-day cumulative GPP composites as a gridded Level 4 dataset at 1-km spatial resolution in the MODIS Sinusoidal projection. MOD17 GPP is estimated using a classic light-use efficiency (LUE) approach in which plant carbon uptake is assumed proportional to canopy-absorbed photosynthetically active radiation (APAR), scaled by a biome-specific maximum efficiency and environmental stress scalars, particularly under low temperature and high vapor pressure deficit (VPD) conditions ([Madani et al., 2017](#); [Running et al., 2004](#); [Yuan et al., 2014](#)).

FluxSat Gross Primary Productivity data: FluxSat global gross primary production dataset is generated from the reflectance data from MODIS, and eddy covariance measurements using machine learning ([Joiner and Yoshida, 2020](#)). Neural networks are trained on MODIS reflectance data to upscale GPP measured with eddy covariance flux towers to generate FluxSat GPP estimate and employed for large scale applications for estimating GPP and validations in absence of in-situ

data in many studies (Ahmad et al., 2022; Bacour et al., 2019; Lv et al., 2023; Zhang et al., 2023).

MODIS Evapotranspiration: This study used the MODIS MOD16A2 Version 6.1 (Running et al., 2021) evapotranspiration 8-day composite estimates at 500-m spatial resolution for evaluating model ET outputs. In MOD16A2, evapotranspiration and latent heat fluxes are derived using a Penman–Monteith–based approach that integrates daily meteorological reanalysis inputs with MODIS remote-sensing products describing vegetation dynamics, surface albedo, and land cover.

GLEAM Evapotranspiration data: The 0.25° daily Global Land Evaporation Amsterdam Model (GLEAM version 3.0a; Miralles et al., 2011) evapotranspiration data is a Priestley Taylor evaporation model product, mainly derived from passive microwave remote sensing. It is developed by combining a wide range of currently existing satellite-sensor products to estimate reliable fields of daily global evaporation and used here to evaluate the modeled evapotranspiration.

Although the above datasets are not direct in-situ measurements, they represent the most widely used observation-based benchmarks for large-scale evaluation of GPP and ET, particularly in data-scarce regions. Efforts have been made for the extensive search for ground-based eddy covariance flux tower observations over South Asia, including publicly available networks such as FLUXNET2015, AsiaFlux, and published site-level studies. However, the spatial coverage of long-term, continuous flux tower measurements within the study domain was found to be extremely sparse, with most sites either located outside the region of interest, or not providing simultaneous measurements of both carbon and water fluxes required for this analysis. In the absence of sufficiently dense flux tower coverage over South Asia, these products provide a consistent and physically interpretable basis for model evaluation at the spatial and temporal scales considered in this study. A list of published works that evaluated the performance of these datasets from global to regional scales and the relevant performance metrics have been reported in Table S2 of supplementary material.

2.4. Model description: Indian land data assimilation system (ILDAS)

ILDAS is an integrated land surface modelling and data assimilation framework specifically designed and configured for South Asia (Magotra et al., 2024a,2024b) developed using the NASA Land Information System Framework (LISF) (Kumar et al., 2006, 2008; Peters-Lidard et al., 2007), Version 7.4. ILDAS is capable of giving reliable estimates of various water storage and flux variables like soil moisture, evapotranspiration, terrestrial water storage, channel discharge and runoff along with floodplain inundation over South Asia. Recently, it has been extended to perform satellite soil moisture data assimilation (Chakraborty et al., 2024). ILDAS supports the usage of multiple local and global meteorological forcing datasets to provide spatially consistent estimates of various land surface state variables at resolution of $0.1^\circ \times 0.1^\circ$.

In this study, all the land surface state variables have been estimated by simulating the Noah-Multiparameterization (Noah-MP) Land Surface Model, (Niu et al., 2011; Yang et al., 2011) Version 4.0.1. Noah-MP considers soil depth of 2 m with four layers and includes various multi-physics options like vegetation, runoff and groundwater dynamics (Nie et al., 2018; Niu et al., 2011; Yang et al., 2011). The geophysical parameters used as inputs for the land surface model have been collected from the different sources as specified in Table 2 following (Chakraborty et al., 2024). The NASA Land Data Toolkit (LDT; Arsenault et al., 2018) has been used to generate the input file by incorporating the model parameters.

In this study, instead of using static vegetation parameters, a prognostic vegetation module introduced by Dickinson et al., (1998a), (1998b) has been enabled in conjunction with a Ball-Berry photosynthesis-based stomatal resistance scheme developed by Ball et al., (1987) and further used in Bonan, (1996) and Collatz et al., (1991), along with the existing model configuration to incorporate the

Table 2

List of input parameters for Land Surface Model, their sources and resolution.

Geophysical Parameters	Data Sources	Resolution
Landcover	MODIS IGBP classes modified by NCEP (Friedl et al., 2002)	0.0833°
Soil texture	FAO derived soil texture map by NCAR	5 min
Elevation, Slope, Aspect	Multi-Error-Removed Improved-Terrain (MERIT) Digital Elevation Model (Yamazaki et al., 2017)	1 km
Albedo	National Centers for Environmental Prediction (NCEP) (Robinson and Kukla, 1985)	1°
Greenness	NCEP (Gutman and Ignatov, 1998)	0.15°
Max snow albedo	Barlage Native (Barlage et al., 2005)	0.05°
Bottom temperature	ISLSCP-1 temperature derived map by NCEP	1°

simulation of carbon cycle and evaluation of carbon flux. These two schemes enable the model to incorporate processes like carbon assimilation via photosynthesis and distribution of that carbon among various canopy components (leaf, stem, root etc.) as well as respiration from each of them. Once stomatal conductance is determined, Noah-MP calculates photosynthesis rates following Farquhar Model (Farquhar et al., 1980) and Collatz et al., (1991).

The current modeling scheme considers generic natural vegetation including generic croplands based on MODIS land cover types to run the carbon dynamics in the model. Noah-MP uses two-stream canopy radiative transfer schemes based on the approximation of Dickinson, (1983) and Sellers (1985) to calculate fluxes absorbed by vegetation, reflected by vegetation, and transmitted through vegetation for unit incoming direct or diffuse flux given an underlying surface with known albedo. More details can be found in He et al., (2023); Niu et al., (2011); Yang et al., (2011).

The leaf respiration and senescence are dependent on the soil water stress (W_{stress}) which is calculated as below:

$$W_{stress} = 1 - \sum_{i=1}^{N_{root}} F_{soil,transp(i)} \quad (1)$$

Where $F_{soil,transp(i)}$ is the transpiration reduction factor of soil layer i , computed from the stomatal resistance formulation and bounded between 0 (fully stressed) and 1 (no stress); N_{root} is the number of soil layers contributing to root water uptake depending on Plant Functional Type (PFTs), enlisted in Table S5 of supplementary material. The soil water stress ranges between 0 (saturated) to 1 (wilting). The leaf carbon mass is calculated using the following equations:

$$M_{leaf} = \max(LAI, 0.05) \times \frac{1000}{\max(1, SLA)} \quad (2)$$

$$M_{leaf,min} = LAI_{min} \times \frac{1000}{SLA} \quad (3)$$

Where, LAI is the leaf area index, M_{leaf} is the leaf carbon mass ($g.C/m^2$) and $M_{leaf,min}$ is the minimum allowed leaf carbon mass, SLA is the single sided leaf area per mass (m^2/kg) (enlisted in Table S5 of supplementary material). Before biomass growth, assimilated carbon is reduced by maintenance respiration, representing metabolic costs of sustaining existing tissues:

$$R_{leaf} = R_{leaf,maint,25C} \times T_f \times F_n \times LAI \times R_{f,reduction} \times (1 - W_{stress}) \quad (4)$$

$$R_{leaf,maint} = \min\left(\frac{M_{leaf} - M_{leaf,min}}{\Delta t}, R_{leaf} \times 12 \times 10^{-6}\right) \quad (5)$$

T_f is the temperature factor, F_n is the foliage nitrogen factor $R_{f,reduction}$ is the respiration reduction factor (=0.5 for non-growing season; 1 for growing season). $R_{leaf,maint,25C}$ is the leaf maintenance respiration rate at 25°C (enlisted in Table S5 of supplementary material). The equations to

calculate T_f , F_n are explained in the [supplementary material](#).

The rate of total carbon assimilation is calculated as:

$$C_{assim,tot} = P_{SN,tot} \times 12 \times 10^{-6} \quad (6)$$

Where, $P_{SN,tot}$ is the total photosynthesis rate. The carbon allocated to leaves are calculated as:

$$C_{assim,leaf} = C_{assim,tot} \times F_{leaf} \quad (7)$$

Where, F_{leaf} is the fraction of carbon flux allocated to the leaf, which is calculated as:

$$F_{leaf} = e^{[0.01 \times LAI \times (1 - e^{\alpha \times LAI})]} \quad (8)$$

Where α is a vegetation type dependent parameter based on the type of land cover. For all vegetation categories α is set to 0.75 (except for evergreen broadleaf forest $\alpha = 0.5$) as per MODIS classification.

The fraction of carbon flux allocated to the stem (F_{stem}) is calculated as:

$$F_{stem} = \frac{LAI}{10} \times F_{leaf} \quad (9)$$

Then F_{leaf} is further updated by subtracting F_{stem} from it. The fractions of carbon flux allocated to the roots are calculated as:

$$F_{root} = (1 - F_{leaf} - F_{stem}) \times (1 - frac_{wood}) \quad (10)$$

Where $frac_{wood}$ is the wood carbon fraction in wood and root pools (further explained in [supplementary material](#)). The turnover rates for different vegetation components are calculated as:

$$T_{leaf} = C_{turn,leaf} \times 5 \times 10^{-7} \times M_{leaf} \quad (11)$$

$$T_{stem} = C_{turn,leaf} \times 5 \times 10^{-7} \times M_{stem} \quad (12)$$

$$T_{root} = C_{turn,root} \times M_{root} \quad (13)$$

Where $C_{turn,leaf}$ and $C_{turn,root}$ are leaf and root turnover rate coefficients respectively (values are specified in [Table S5](#) of [supplementary material](#)). M_{stem} and M_{root} are the stem and root carbon mass (initialized to 500.0 g.C/m²).

The seasonal death rate or senescence due to temperature and water stresses are calculated as below:

$$S_{cd,leaf} = M_{leaf} \times (F_{td} \times C_{td} + F_{wd} \times C_{wd}) \times 10^{-6} \quad (14)$$

$$S_{cd,stem} = M_{stem} \times (F_{td} \times C_{td} + F_{wd} \times C_{wd}) \times 10^{-6} \quad (15)$$

Where, F_{td} and F_{wd} are death coefficients due to temperature and water stresses respectively, C_{td} and C_{wd} are the temperature and water coefficients for leaf death respectively. The calculations of F_{td} and F_{wd} and the values of C_{td} and C_{wd} are explained in the [supplementary material](#).

The total gross primary productivity (GPP, g.C/m²/s) is obtained as diagnostic output:

$$GPP = C_{assim,tot} \quad (16)$$

The specific leaf area, a metric that depends on the type of vegetation, is multiplied by the leaf carbon mass to get the leaf area index (LAI). LAI and SAI get further updated as:

$$LAI = \max\left(LAI_{min}, M_{leaf} \times \frac{SLA}{1000}\right) \quad (17)$$

$$SAI = \max\left(SAI_{min}, M_{stem} \times \frac{3}{1000}\right) \quad (18)$$

The Green Vegetation Fraction (GVF) is determined by partitioning a grid cell into a fractional area covered by vegetation and a fractional area of bare land. This partitioning is based on the Leaf Area Index (LAI)

and is calculated using the following mathematical function:

$$GVF = 1 - e^{-0.52LAI} \quad (19)$$

GVF is a crucial factor in Noah-MP, responsible for accurately representing vegetation status and distributing evapotranspiration into multiple components. The GVF value for each tile is set to the maximum value of all months from the monthly climatology at that tile. This scheme enables the model to estimate GPP as diagnostic output in addition with the ET estimates from the default model setup of ILDAAS (Chakraborty et al., 2024; Magotra et al., 2024a,2024b). Further details of this dynamic vegetation scheme and related biochemical processes can be found in He et al., (2023); Niu et al., (2011); Yang et al., (2011). As ILDAAS does not give WUE directly as diagnostic output variable, both GPP and ET from model estimates are used to calculate the ecosystem WUE as ratio of GPP and ET.

The entire methodology and model setup has been described in [Fig. 2](#).

2.5. Experimental setup

The Noah-MP land surface model was spun up for four cycles, each spanning five years (from 1st January 1980–31 st December 1984), giving spin ups for a total 20-year period to establish stable and steady-state initial conditions within ILDAAS by taking the meteorological forcing variables as listed in [Table 1](#) and the model input parameters for the selected domain as specified in [Table 2](#). During each spin-up cycle, the model was forced with consistent meteorological inputs to allow the key land surface state and flux variables to reach equilibrium, minimizing any transient effects in the simulations. Key parameters such as soil moisture, ET, runoff and vegetation states were monitored to confirm that variations stabilized after each spin-up cycle, indicating model stability. Convergence was assessed by quantifying the change in key state variables between successive cycles using (i) the 5-year mean fields and (ii) domain-wide statistics (median and 95th-percentile of absolute cycle-to-cycle differences). The list of those monitored variables along with their respective convergence thresholds and the results of convergence curves are described in [Table S3](#) and [Fig S1](#) of [supplementary material](#).

Following the spin-up phase, a continuous simulation from 1st January 1985–31 st December 2023 was conducted to capture long-term variability. The different physics options used in the land surface model configuration for both spin up and main simulations are described in [Table S4](#) of the [supplementary material](#). The meteorological forcings for all these simulations have been taken from two different forcing data sources: IMD precipitation with other forcing variables from MERRA2, as specified in [Table 1](#). The purpose is to incorporate local precipitation dataset along with the other global forcings for the model to capture the local variation precisely. To ensure consistent integration across national and transboundary areas, different precipitation datasets were harmonized by defining boundary protocols: within Indian national borders, the model applied IMD precipitation data in combination with MERRA2 forcings, while outside the Indian national boundary, MERRA2 precipitation data was utilized to maintain continuity. LIS setup is being configured here to use two meteorological forcing sources with the blending option as “overlay”. The global MERRA-2 meteorological fields specified in [Table 1](#) are read using the built-in MERRA2 forcing readers. Within LIS, the overlay blending method gives precedence to the IMD precipitation data generated in LDT format. Consequently, IMD precipitation from the LDT-generated forcing is used wherever it is defined (over India), and MERRA-2 precipitation is used elsewhere; all non-precipitation variables are taken exclusively from MERRA-2.

2.6. Trend, sensitivity analysis, and validation

For analyzing the long-term trends in annual GPP and WUE time

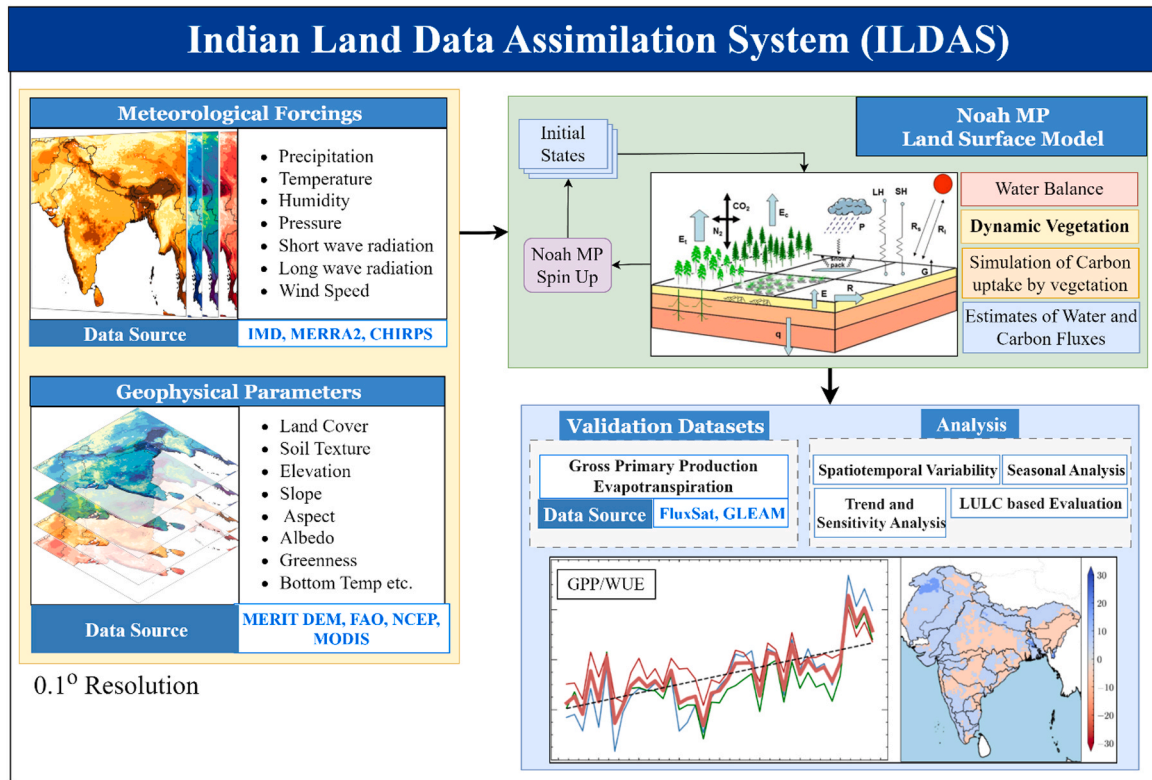


Fig. 2. Methodology for dynamic vegetation simulation along with land surface model within ILDA.

series, a combination of non-parametric trend detection and robust slope estimation techniques was applied. Since monotonic trend tests such as the classical Mann–Kendall (MK) test assumes serial independence of observations, and the GPP or WUE time series may typically exhibit strong autocorrelation due to ecosystem carbon pool memory effects, an explicit assessment of temporal autocorrelation was conducted prior to trend estimation using the sample lag-1 autocorrelation coefficient:

$$\rho_1 = \frac{\sum_{t=2}^n (x_t - \bar{x})(x_{t-1} - \bar{x})}{\sum_{t=1}^n (x_t - \bar{x})^2} \quad (20)$$

where x_t represents the annual time series, \bar{x} is the sample mean, and n is the total number of years. Following standard practice, the time series was considered significantly autocorrelated when $\rho_1 > \frac{2}{\sqrt{n}}$. If $\rho_1 \leq \frac{2}{\sqrt{n}}$, the series is considered as serially independent and suitable for the application of the classical Mann–Kendall test (Mann, 1945). However, if significant autocorrelation exists then the classical MK test is inappropriate due to its tendency to underestimate variance and inflate the significance of trend. In such cases, the Modified Mann–Kendall (MMK, Hamed and Ramachandra Rao, 1998) test is suitable. The Modified Mann–Kendall test retains the original Mann–Kendall S-statistic but corrects its variance to explicitly account for serial correlation. It also operates as a rank-based significance test like the classical one, assessing whether the S-statistics of the time series fall within the confidence interval, thereby determining the significance of the observed trend under the null hypothesis. If x_i and x_j are the values in the time series at times i and j , respectively and n is the total number of observations, then S statistic is calculated as:

$$S = \sum_{i=1}^{n-1} \sum_{j=i+1}^n \text{sgn}(x_j - x_i) \quad (21)$$

Where sgn is the sign function defined as below:

$$\text{sgn}(x_j - x_i) = \begin{cases} +1, & \text{if } x_j - x_i > 0 \\ 0, & \text{if } x_j - x_i = 0 \\ -1, & \text{if } x_j - x_i < 0 \end{cases} \quad (22)$$

The Modified Mann–Kendall test introduces an effective sample size n^* to account for autocorrelation, defined as:

$$n^* = \frac{n}{1 + 2 \sum_{k=1}^{n-1} \left(1 - \frac{k}{n}\right) \rho_k} \quad (23)$$

Where ρ_k is the lag- k autocorrelation coefficient of the time series. In practice, the summation is truncated to statistically significant lags, with lag-1 autocorrelation often dominating annual ecosystem time series. The corrected variance of the S-statistic is then computed as:

$$\text{Var}^*(S) = \text{Var}(S) \times \frac{n}{n^*} \quad (24)$$

This variance inflation directly reduces the likelihood of falsely detecting significant trends in autocorrelated data. The standardized Z-statistic is subsequently calculated using the corrected variance:

$$Z = \begin{cases} \frac{S-1}{\sqrt{\text{Var}^*(S)}}, & S > 0 \\ 0, & S = 0 \\ \frac{S+1}{\sqrt{\text{Var}^*(S)}}, & S < 0 \end{cases} \quad (25)$$

The null hypothesis of no monotonic trend is rejected if $|Z|$ exceeds the critical value corresponding to the chosen significance level ($p = 0.05$ in this study).

The long-term trends in the GPP and WUE have been quantified by determining the Theil–Sen slope (Sen, 1968) using the following equation:

$$\text{Slope}_{TS} = \text{median} \left[\frac{(x_j - x_i)}{(j - i)} \right] \quad (26)$$

Where x_j and x_i are the data values at j^{th} and i^{th} time step, respectively. The significance of the slope has been estimated from the Mann-Kendall test p-value and compared with the level of significance chosen (0.05 here) to evaluate with respect to the null hypothesis. To better characterize trend robustness, uncertainty ranges for the Theil–Sen slope were estimated and reported as confidence intervals alongside the median slope values. Reporting both slope magnitude and associated uncertainty provides a more reliable assessment of long-term ecosystem trends.

The sensitivity analysis of WUE with respect to all the forcing variables enlisted in Table 1 and different other LSM estimated variables such as soil moisture (SM), evapotranspiration (ET), and leaf area index (LAI) have been performed to observe their influence on the WUE estimates. Prior to performing the sensitivity analysis, the statistical distribution of these variables has been analyzed in terms of standardized Z-score to assess their suitability for different analytical approaches

$$Z = \left[\frac{X - \mu}{\sigma} \right] \quad (27)$$

Where, X is the variable, μ is the mean and σ is the standard deviation.

The boxplots of the standardized Z-scores in Fig. S2 of the supplementary material reveal considerable dispersion and skewness in the distributions of these variables, especially for precipitation, windspeed, and evapotranspiration, as well as the presence of noticeable outliers in most of the variables. These statistical characteristics indicate the violation of assumptions of normality and homoscedasticity required for parametric methods sensitivity of tests. Under such circumstances, a non-parametric elasticity method (Schaafe and Waggoner, 1990) is chosen to assess the sensitivity of Water Use Efficiency (WUE) to all those influencing variables. This approach is selected over parametric methods because it offers greater robustness against outliers and is well-suited for non-linear relationships, which are common in complex land surface interactions and applied in hydro-meteorological sensitivity analyses (Konapala and Mishra, 2016; Liu et al., 2017, 2020; Veettil et al., 2018). This elasticity (ε) test has been employed here to observe the influence of the mentioned variables on WUE. Based on the theory of elasticity, ε was defined as:

$$\varepsilon = \text{median} \left\{ \frac{(X_i - \bar{X})/\bar{X}}{(Y_i - \bar{Y})/\bar{Y}} \right\} \quad (28)$$

Where, X_i , Y_i denote the WUE and the influencing variable respectively and \bar{X} , \bar{Y} denote their respective long-term averages. The median-based approach minimizes the effect of outliers, providing a reliable sensitivity measure even when extreme values are present. Before applying the elasticity method, each variable was resampled to a common temporal resolution, and missing values were interpolated where necessary to maintain data continuity. This preprocessing ensured that elasticity estimates accurately reflected the relationship between WUE and the selected variables, supporting reliable interpretations of sensitivity. However, this approach also has limitations. Because elasticity is computed using median proportional deviations, it primarily characterizes the central tendency of the WUE response. It may therefore under-represent highly nonlinear, state-dependent, or threshold-driven responses, and does not explicitly describe tail-dominated dynamics driven by extremes. These considerations are taken into account in interpreting the results.

The model outputs of GPP and ET are validated against the observed datasets mentioned in 2.3, using the standard statistical metrics such as Correlation (R) and Kling-Gupta Efficiency index (KGE; Gupta and Kling, 2011).

$$R = \left[\frac{\Sigma(O - \mu_o)(S - \mu_s)}{\sqrt{\Sigma(O - \mu_o)^2} \sqrt{\Sigma(S - \mu_s)^2}} \right] \quad (29)$$

$$KGE = 1 - \sqrt{S_r[R - 1]^2 + S_\alpha[\alpha - 1]^2 + S_\beta[\beta - 1]^2} \quad (30)$$

Where, O represents the observed variable, S represents the simulated variable, $\alpha = \frac{\sigma_s}{\sigma_o}$, $\beta = \frac{\mu_s}{\mu_o}$, S_r , S_α , and S_β are scaling factors for the three components, respectively, which are specified by the user; σ_s and σ_o are the standard deviations for simulated and observed variables, respectively, and μ_s and μ_o are the corresponding mean values. Employing these basic equations we also evaluated the climatological and anomaly correlations, climatological amplitude ratio ($\alpha_{clim} = \frac{\sigma_{s,clim}}{\sigma_{o,clim}}$) that evaluates the seasonal cycle amplitude of the simulated variable with that of the observed variable, and the anomaly standard deviation ratio ($\alpha_{anom} = \frac{\sigma_{s,anom}}{\sigma_{o,anom}}$) that measures how well the model reproduces the inter-annual variability after removing the climatological mean.

3. Results and analysis

3.1. Spatiotemporal variability

To observe the overall spatial variability of GPP, ET and WUE over the study domain, mean annual spatial maps of GPP (Fig. 3, a), ET (Fig. 3, b) and WUE (Fig. 3, c) over the domain are shown.

One common pattern of variation can be observed for all the three variables, especially over the lower Himalayan region and north-eastern hilly regions, mainly characterized by medium to dense forest cover, exhibit consistently high values of GPP ($>2500 \text{ g.C/m}^2/\text{year}$), ET ($>900 \text{ mm/year}$) and WUE ($>2 \text{ g.C/kg H}_2\text{O/year}$). This is signifying the importance of forest lands in contributing towards ecosystem productivity. Because natural vegetations like forest covers can assimilate atmospheric carbon proportional to greening. Whereas upper Himalayan region characterized by snow/ice and barren land has less GPP and ET, resulting in less values of WUE over that region. A diverging spatial variation of these parameters can be observed over the Brahmaputra basin. Interestingly, lower Brahmaputra basin has higher GPP, ET and WUE.

Fig. 3(d) further disaggregates WUE by river basins, showing the variability in monthly WUE across 18 major river basins. The Brahmaputra and Subarnarekha basins show the highest median WUE values ($>2 \text{ g C/m}^2/\text{mm}$). In contrast, the Indus, Krishna, and Penner basins display the lowest WUE ($<1.5 \text{ g C/m}^2/\text{mm}$). The interquartile range (IQR) for each basin also highlights the seasonal and interannual variability in WUE, particularly in monsoon-dominated catchments such as the Ganges, Godavari, and Mahanadi.

3.2. Variation across different seasons and land covers

The seasonal variations in GPP, ET and WUE can be contrasted further spatially by observing seasonal maps (Fig. 4). The Indian sub-continent region is mainly dominated by four major seasons: Pre-Monsoon (March to May), Monsoon (June to September), Post-Monsoon (October to November) and Winter (December to February). The seasonal variations show that GPP, ET and WUE values are high especially over eastern and north-eastern India along with the lower Himalayan region consistently in all the seasonal maps. However, GPP show high spatial variability during the monsoon and post-monsoon season having the values of standard deviation, $\sigma = 95.44 \text{ g C/m}^2$ and $\sigma = 88.39 \text{ g C/m}^2$ respectively. In fact, high GPP values can be observed over most of the domain during the post-monsoon season. This reflects substantial regional gradients in rainfall and vegetation productivity. The spatial variability in WUE during this period remains lower ($\sigma =$

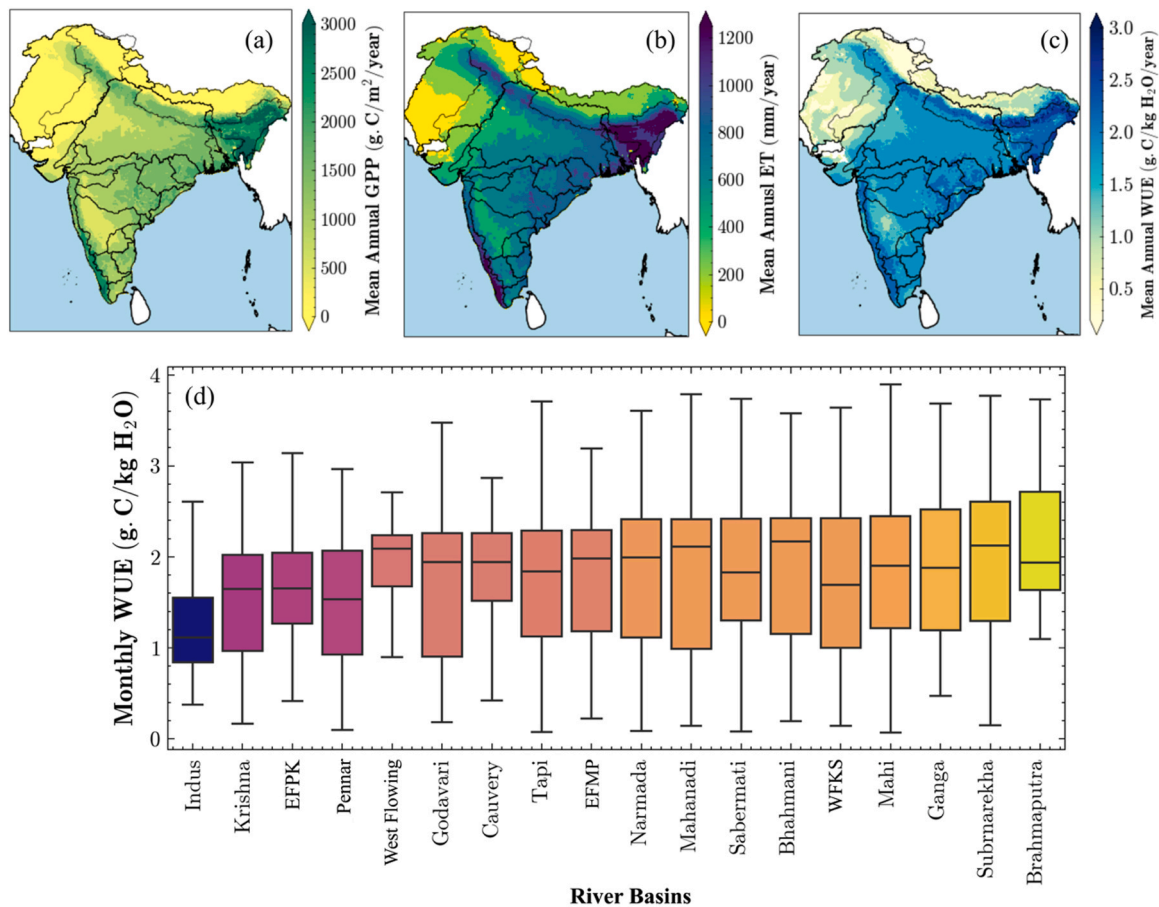


Fig. 3. Spatial maps showing variations in mean annual (a) GPP, (b) ET and (c) WUE, for the period 1985–2023. (d) Box plots showing basin wise distribution of monthly WUE for the same time period.

1.04 g C/m²/mm).

On the contrary, the pre-monsoon and winter seasons exhibit relatively lower spatial variability in GPP and ET yet records moderate to high in WUE ($\sigma = 8.63\text{--}12.48$ g C/m²/mm), indicating enhanced water-use efficiency, which can be attributed to stomatal regulation of plants in water limited conditions, leading to the efficient usage of water. However, throughout the year, lower Himalayan belt covering north-eastern region shows high values of GPP, ET and WUE.

These estimates may vary over different places, especially land covers during different seasons and months. Based on the classified land cover pixels from the input dataset, the seasonal statistical distributions of GPP, ET and WUE have been evaluated for all these land cover classes (Fig. 5).

For GPP and ET, almost all the land covers show similar pattern of seasonal variation: minimum during pre-monsoon season, reaches to maximum during monsoon season and then keep decreasing from post-monsoon to winter season. But in case of WUE, it keeps increasing from pre-monsoon to winter season except shrublands and snow-ice and barren lands. WUE drops down to minimum in monsoon season in case of shrublands and then increases. For snow and barren lands, WUE increases slightly during monsoon and post-monsoon season and drops down again during winter season.

Overall, in terms of the land cover wise distribution, forest lands show highest GPP and ET, however, shrublands characterized by semi-arid region with sparse vegetation cover shows high WUE even having lower GPP and ET. Croplands are found to contribute less towards WUE in comparison to other vegetations, despite showing higher greening due to expansion over the domain.

3.3. Sensitivity analysis of WUE

The sensitivity analysis of WUE is performed with respect to various meteorological forcings specified in Table 1. Fig. 6 shows the scatter plots of WUE with respect to other selected meteorological forcing drivers or variables along with their sensitivity in terms of the non-parametric elasticity values, quantifying the strength and direction of influence of each variable on WUE, indicated using the color scale.

Higher the elasticity value (positive or negative), more sensitive the variable is towards WUE. However, the positive elasticity values (shown in blue) indicate a direct relationship, where WUE tends to increase with the increase in the respective variable, whereas negative values (shown in red hues) suggest an inverse relationship, where WUE decreases as the variable increases. Median elasticity values are shown within each subplot, to summarize measure of central tendency of sensitivity. WUE shows strong negative elasticity with near-surface air temperature (median $\epsilon = -21.78$), followed by longwave (median $\epsilon = -2.30$) and shortwave radiation (median $\epsilon = -2.23$) respectively, implying that increases in these variables are typically led to a reduction in WUE. This observation aligns with the understanding that higher temperatures lead to greater evaporative demand, indicates that warming substantially reduces WUE, primarily through increased VPD and stomatal closure, which suppress carbon assimilation more strongly than ET. Conversely, atmospheric pressure (median $\epsilon = 76.30$) shows quite stronger positive elasticities, suggesting that increased pressure may enhance WUE under certain hydroclimatic conditions. Although pressure is not a direct physiological control, it acts as a proxy for high-pressure synoptic regimes characterized by subsidence, clear skies, and strong stomatal regulation. This interpretation is supported by recent studies linking

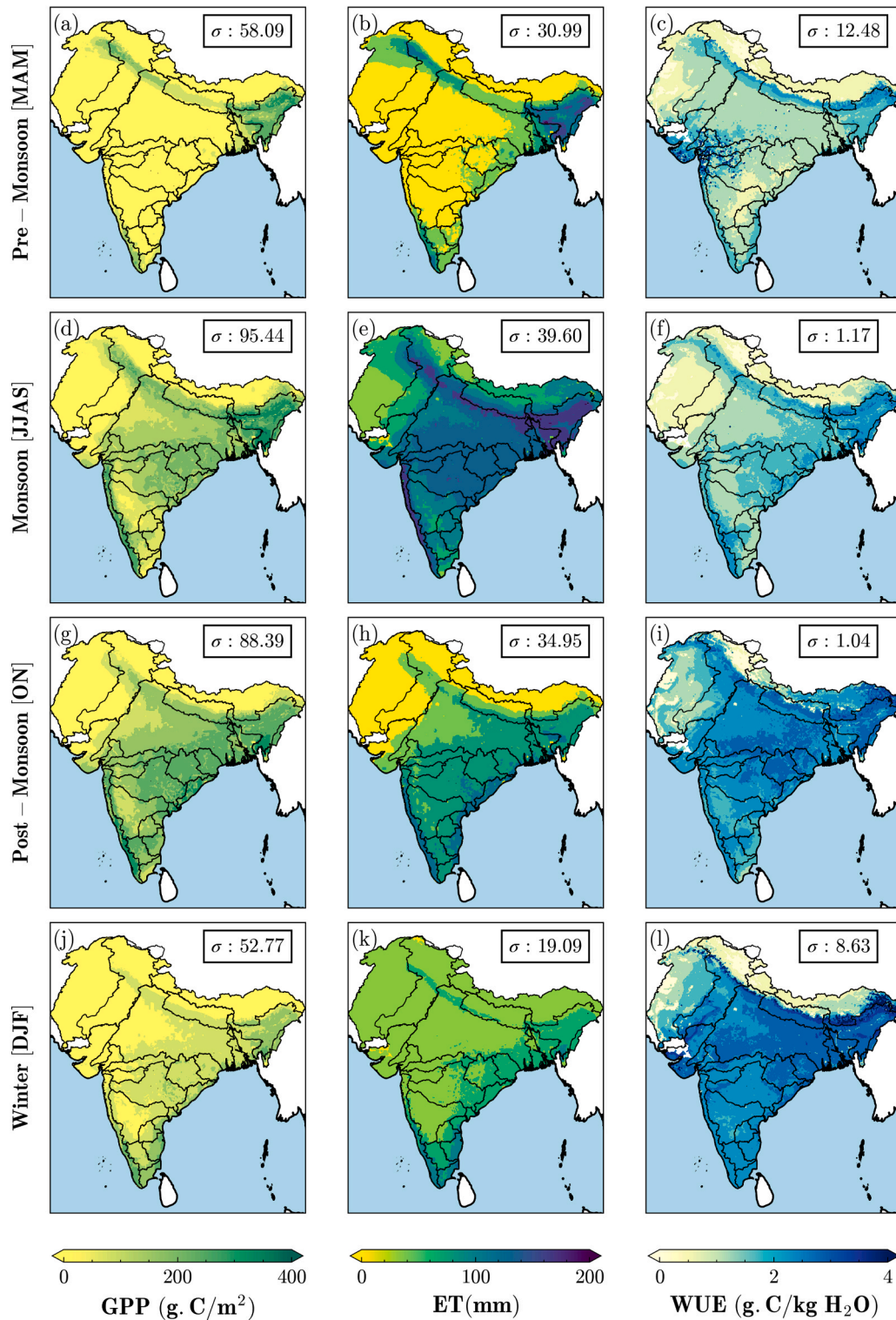


Fig. 4. Seasonal maps showing spatial distribution of Gross Primary Productivity (GPP), Evapotranspiration (ET), and Water Use Efficiency (WUE) across South Asia for the period 1985–2023. Each row corresponds to a different season: (a–c)Pre-Monsoon, (d–f)Monsoon, (g–i)Post- Monsoon, and (j–l)Winter. The accompanying values (σ) in each panel represent the spatial standard deviation of the respective variable, reflecting intra-seasonal spatial variability.

high-pressure, dry meteorological regimes to altered plant gas exchange and energy flux dynamics (C. Li et al., 2025; Y. Li et al., 2025; Zhang et al., 2019). In fact, it also reflects elevation-dependent gradients in climate and vegetation structure rather than a direct physiological response to atmospheric pressure. WUE is found less sensitive to precipitation, humidity and windspeed.

A similar kind of analysis is also shown in Fig. 7 for observing the sensitivity of WUE towards the LSM estimated state variables: soil moisture (SM), ET and LAI.

In case of SM and ET, the positively sensitive points are clustered at lower WUE region between 0 and 1 g C/m²/mm. In such clusters, soil moisture ranges from 0 to 0.2 m³/m³ and ET between 40 and 60 mm.

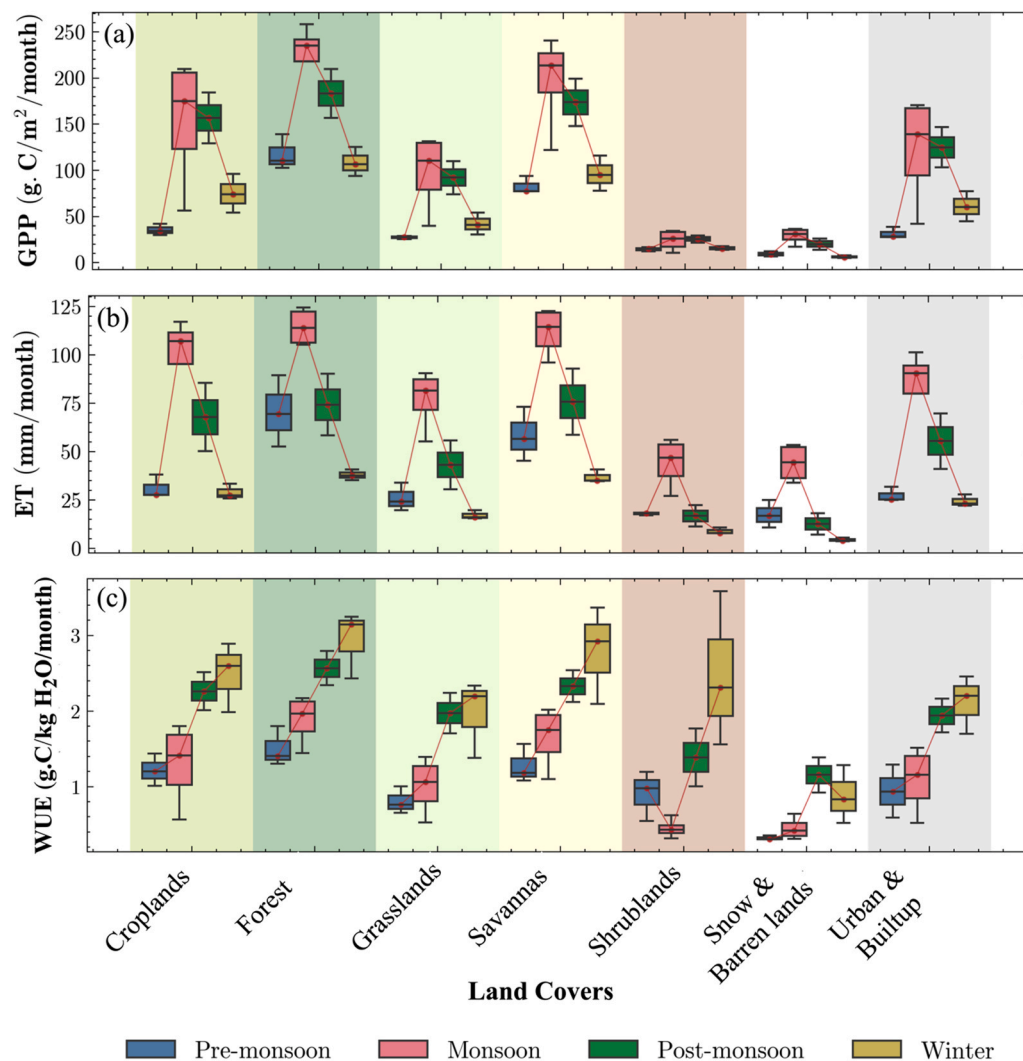


Fig. 5. Seasonal box plots of monthly climatological mean (a) GPP, (b) ET and (c) WUE for different land covers, for the period 1985–2023.

That means at lower values of WUE ($0\text{--}1\text{ g C/m}^2/\text{mm}$), it is positively sensitive to SM and ET which indicates that WUE significantly increases with the increase in these parameters. This actually indicates a moisture-threshold behavior (Fu et al., 2024; Zhou et al., 2014, 2015). Under low WUE conditions (representing water-limited states typically corresponding to pre-monsoon and semi-arid conditions), increases in soil moisture and ET alleviate stomatal constraint and substantially enhance photosynthetic activities relative to transpiration, resulting in a positive WUE sensitivity. On the other hand, at higher WUE ranges ($2.5\text{--}3\text{ g C/m}^2/\text{mm}$), WUE is negatively sensitive to SM, ET as well as LAI. This thing is evident from the negatively sensitive clusters observed at higher WUE ($2.5\text{--}3\text{ g C/m}^2/\text{mm}$), indicating at that range of WUE, increase in SM or ET or LAI, leading to decrease in WUE. At higher WUE ranges, ecosystems enter moisture-sufficient states, where photosynthetic gains saturate while transpiration continues to rise with increasing SM, ET or canopy development (LAI). This likely leads to declining marginal carbon gain per unit water loss, producing negative elasticity. This regime-dependent response is consistent with ecohydrological functioning of South Asian monsoon and irrigated agro-ecosystems.

In case of LAI, WUE is positively sensitive when both WUE and LAI increases. Whereas sensitivity is negative when both LAI and WUE values are less. Based on absolute values of sensitivity (both positive and negative), WUE is observed to be more sensitive to soil moisture and LAI than ET. Because LAI and soil moisture are the key indicators of the

vegetation condition of a region. Variability in soil moisture and LAI influences the plant carbon uptake and water availability for canopies, hereby influencing ecosystem WUE.

To further analyze this impact spatially, the absolute spearman's correlation values between those variables and the WUE is observed for each land cover type which indicates the strength of monotonic association between WUE and an individual variable, irrespective of direction (i.e., focusing on sensitivity rather than sign and shown in terms of land cover wise bar plots in Fig. S3 in the supplementary material. For most of the land cover types, temperature, radiation and pressure are found more consistently influential factors than soil moisture or LAI, suggesting that atmospheric conditions dominate over surface state variability in shaping seasonal WUE patterns.

3.4. Trend analysis of GPP and WUE

The Fig. 8 shows the mean annual variation of GPP (Fig. 8, a) and WUE (Fig. 8, d) over the study domain along with the trend line and a shaded region showing the 95% confidence interval. The results from Theil Sen's slope test with the uncertainty in the estimated slopes are shown in the form of spatial maps (Fig. 8, b, c, e and f). The long-term trend analysis of GPP shows overall increasing trend when compared in terms of domain averaged annual time series (Fig. 8). Overall annual mean GPP ranges in between 800 g C/m^2 to 1400 g C/m^2 based on the last 40 years analysis. These increases in GPP and WUE can be attributed

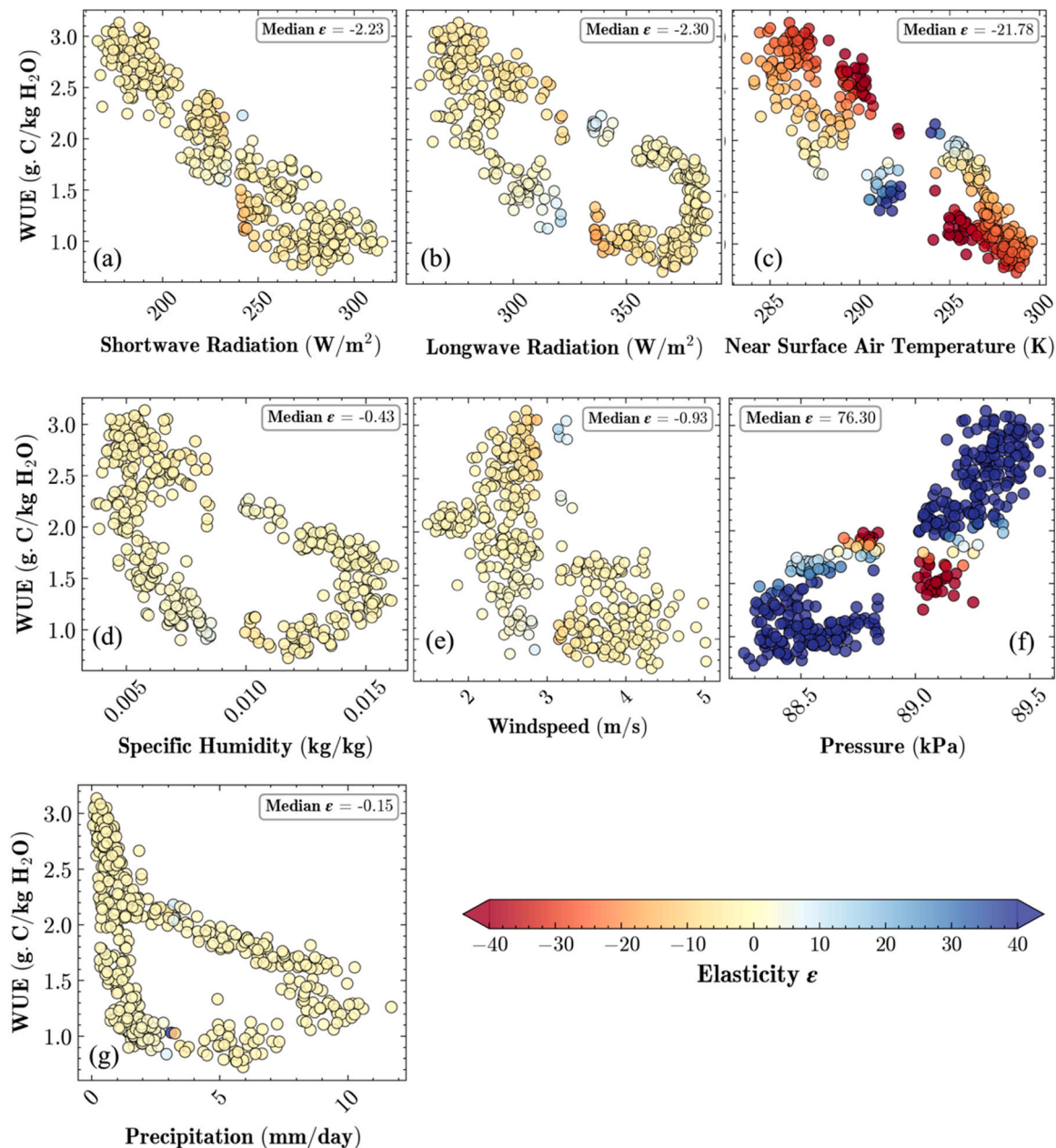


Fig. 6. Scatter plots of sensitive variables with respect to WUE showing the distribution of elasticity in color bar for the period 1985–2023. Median values of elasticity shown in the text boxes for each subplot.

to increasing carbon concentration in the atmosphere due to vegetation greening. The spatial patterns of trend in terms of Theil-Sen slope for 95% significance level ($p < 0.05$) for ensemble mean GPP have been shown in Fig. 8, (b).

A significant increasing trend can be observed over the lower Himalayan region but a decreasing trend over the southern region. Increasing trend in domain average WUE can be observed from the time series plot in Fig. 8, (d). Additionally, annual WUE variation is found within the range of $1.5 \text{ g C/m}^2/\text{mm}$ to $1.8 \text{ g C/m}^2/\text{mm}$. Whereas the spatially significant trend is increasing over the Himalayan belt and some regions of middle India (Fig. 8, e). Significantly decreasing trend can be observed over the north-west and southern India. The corresponding slope uncertainty map (Fig. 8, c & f) indicates relatively low to moderate over most areas, supporting the statistical reliability of the detected spatial patterns.

3.5. Variation and trend of WUE in agro-ecological zones of India

The Indian subcontinent comprises a diversity of Agro-Ecological Zones (AEZs), including humid tropical regions in the Western Ghats to semi-arid zones in Rajasthan and high-altitude Himalayan areas. Each AEZ differs in terms of climatic conditions, soil types, and vegetation compositions from each other, which influences how efficiently ecosystems utilize water for carbon assimilation. To assess whether the assumption of serial independence required by the classical Mann-Kendall (MK) trend test is satisfied, a lag-1 autocorrelation (ρ_1) analysis was conducted for the annual WUE time series for all these AEZs. Fig. S4 of supplementary material shows that many of ecologically important AEZs show significant autocorrelation, with $|\rho_1|$ exceeding the critical threshold ($2/\sqrt{n}$), with median autocorrelation value 0.342 being slightly higher than the threshold (~ 0.32). This indicates that applying the standard MK test could overestimate trend significance and lead to false positives for those AEZs. To account for this serial

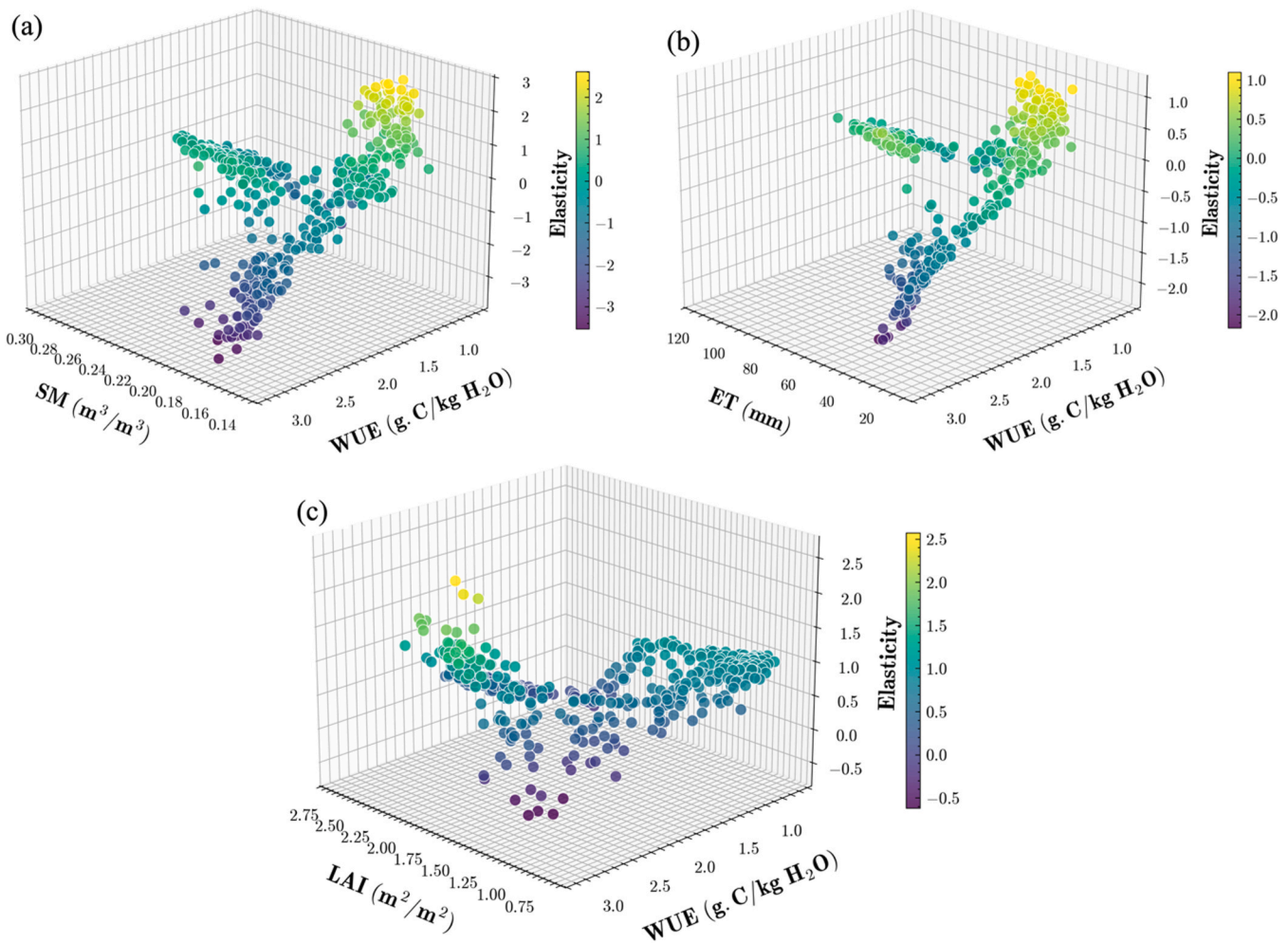


Fig. 7. Scatter plots of distribution and sensitivity of WUE with respect to other LSM estimated variables: (a) soil moisture (SM), (b) evapotranspiration (ET) and (c) leaf area index (LAI) from 1985 to 2023.

dependence, the modified Mann–Kendall test was therefore applied across the entire domain as the S-statistic remains unaffected. To get insights into the trend of WUE and its impact upon different AEZs, the S statistics is shown in Fig. 9, (a).

The lower Himalayan belt along with the highly irrigated Gangetic plane and north-eastern hilly areas with dense forest covers show increasing trend in WUE as confirmed by the S-statistics, due to the presence of dense vegetation cover and having the sufficient availability of water. It shows that the Northern and Central India (e.g., the Indo-Gangetic Plains, Himalayan regions, Central highlands of Gujrat) show stronger increasing trends in WUE. Southern India, especially the Decan Plateau and Western Ghats, has weaker trends. Coastal regions and drier zones (Western Rajasthan, Gujarat) exhibit lower WUE trends.

The box plots in Fig. 9, (b) compares distribution of monthly WUE across different AEZs. The color gradient applied to the boxplots corresponds to mean WUE values, enhancing comparative interpretation across regions. Out of all these 19 AEZs, the zones such as the Eastern Himalayas, North-Eastern Hills, and Assam & Bengal Plains show higher median WUE values and relatively narrower variability, suggesting favorable eco-hydrological conditions for carbon uptake. On the other hand, Western Himalayas (Cold Arid – Zone 17) shows the lowest WUE with extremely low variability, indicating consistent water-limited carbon assimilation across years.

3.6. Statistical analysis and validation

Statistical analysis of model estimated GPP has been performed with respect to MODIS satellite derived GPP and FluxSat GPP data. Fig. 10 (a–d) shows the spatial maps of correlation (R), and KGE for model estimated GPP with MODIS and FluxSat GPP. Overall, the model shows better agreement with FluxSat than with MODIS, as evident from the higher median R (0.70 vs. 0.68) and KGE (0.43 vs. 0.32) values. Moderate to high agreement with both datasets is found over central India, the Indo-Gangetic Plains, eastern India, and much of peninsular India, where croplands and seasonally productive vegetation dominate and monsoon-driven moisture regulates carbon uptake. Model performance is weaker over northwestern India and the upper Himalayan region, which are classified as barren land, snow, or ice in the static land-cover input, leading to suppressed simulated GPP in those regions. In contrast, satellite datasets likely capture episodic greening and sparse vegetation responses, explaining the reduced agreement in these regions.

The land-cover-wise diagnostic metrics (Fig. 10, e–h) further explains the spatial patterns observed in the evaluation maps by separating climatological and anomaly comparisons. Consistent with the higher spatial agreement seen in the maps, the model shows stronger climatological correlation with FluxSat across most of the land-covers, particularly croplands, grasslands, savannas, and urban/built-up areas, better capturing seasonal GPP cycles (Fig. 10, e). In contrast, climatological correlations with MODIS are systematically lower, especially over forests and shrublands, which can be attributed to the differences

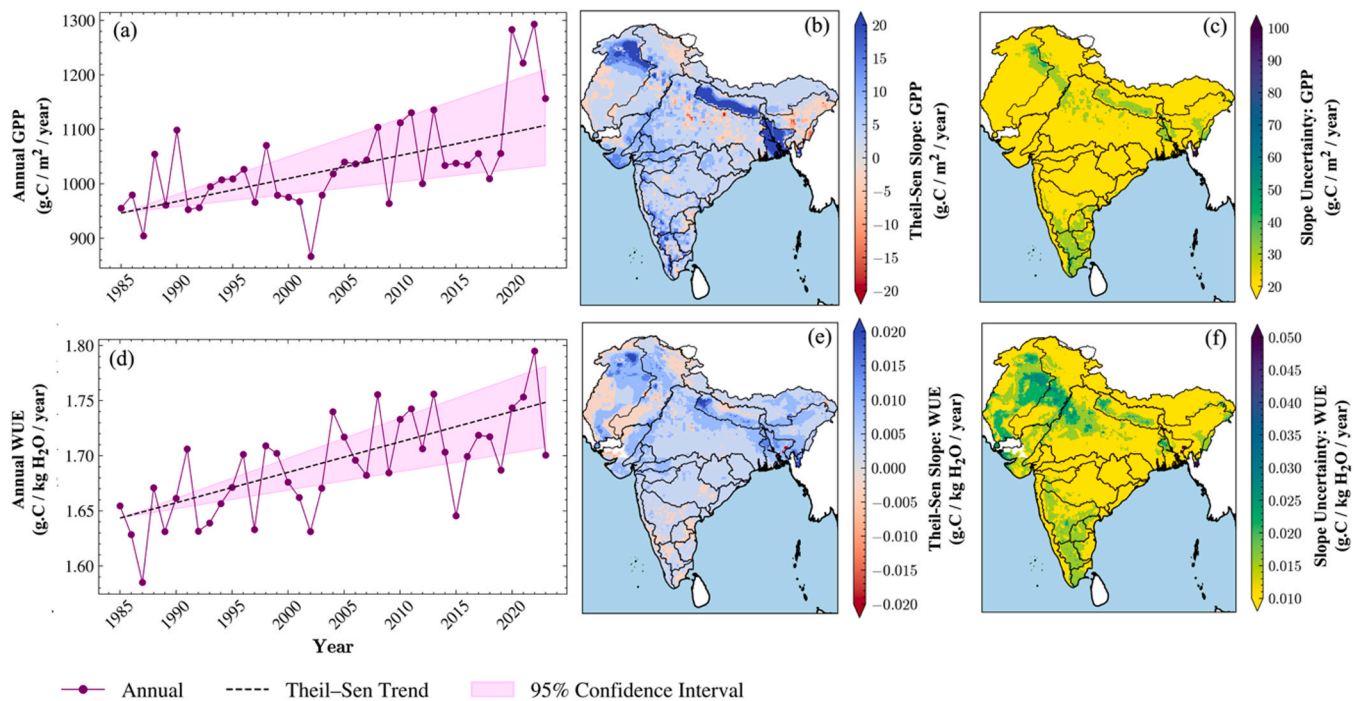


Fig. 8. Trends in GPP and WUE over South Asia: annual time series with Theil–Sen trend and 95% CI for (a) GPP and (d) WUE; spatial Theil–Sen slope maps of (b) GPP and (e) WUE; maps of uncertainty in Theil–Sen slope estimates for (c) GPP and (f) WUE from 1985 to 2023.

between process-based carbon simulations and the light-use-efficiency framework underlying MODIS GPP (Wang et al., 2013, 2025). The climatological amplitude ratio (Fig. 10, f) highlights that the model tends to slightly overestimate seasonal amplitudes relative to FluxSat in forested and savanna regions, while amplitudes are closer to unity for croplands and grasslands. MODIS-based amplitude ratios show larger deviations from unity across several land-cover types, consistent with the lower KGE values seen in the spatial maps.

Anomaly-based metrics further indicate that the model captures interannual variability more consistently with FluxSat than with MODIS across most vegetation classes (Fig. 10, g–h). Higher anomaly correlations and anomaly standard ratios closer to unity for FluxSat suggest improved representation of year-to-year GPP variability, whereas reduced anomaly agreement with MODIS—particularly over forests and arid classes—points to differences in stress response and vegetation sensitivity. Overall, these land-cover-specific diagnostics reinforce the spatial evaluation results, demonstrating that model performance is strongest in climatically active and managed ecosystems and more uncertain in sparsely vegetated or structurally complex regions.

A similar kind of analysis has been done for the model ET estimates in comparison with GLEAM and MODIS ET datasets (Fig. 11).

ET estimates show a different pattern of statistical performance than GPP (Fig. 11). ET estimates are showing better statistical performance over the entire Himalayan region, western and north-east Indian region. The model shows overall stronger agreement with MODIS ET, as reflected by higher median spatial R (= 0.81) and KGE (= 0.44) compared to GLEAM (median R = 0.78; KGE = 0.35) (Fig. 11, a–d). Spatially, across most of the study domain modeled GPP shows high correlation with GLEAM, which is evident across central, eastern and the north-western India. Better agreement with MODIS can be observed in the Indo-Gangetic Plain, and peninsular regions, where ET is strongly governed by vegetation activity and surface energy balance processes explicitly represented in Noah-MP. In contrast, reduced agreement over arid northwestern India and high-elevation Himalayan regions persists, reflecting uncertainties associated with sparse vegetation, soil moisture limitations. Land-cover based diagnostics indicate that while GLEAM captures ET anomalies reasonably well in some classes, MODIS provides

a better overall match in terms of mean state and variability, consistent with its Penman–Monteith formulation that integrates vegetation and meteorological constraints.

Validation shows strong agreement for modeled GPP and ET across most of South Asia, particularly over forests, croplands, and grasslands, where vegetation dynamics and surface processes are likely well represented by the model. Lower R and KGE values in arid, urban, and snow-dominated regions indicate systematic model biases due to challenges in capturing flux magnitude and variability, land-cover heterogeneity and sub-grid processes. Reduced performance in northwestern India and the upper Himalayan region reflects model assumptions of barren land or snow with minimal vegetation activity, while satellite GPP products capture episodic greening and sparse vegetation signals. For ET, agreement with MODIS is weaker, whereas GLEAM shows better consistency, as both emphasize radiation- and moisture-driven evaporation over transpiration in these environments. These differences highlight the structural contrasts between satellite retrieval approaches and process-based model assumptions, particularly in arid and high-elevation environments.

To address the absence of direct WUE observations, the model-derived WUE, defined as the ratio of GPP/ET is evaluated against an independent satellite-based WUE estimate derived from the ratio of MODIS GPP (MOD17A2H) and MODIS ET (MOD16A2). Spatial comparisons were performed using grid-cell-wise time series of monthly WUE over the common evaluation period and resampling to monthly timestep.

Fig. 12 shows the spatial maps of R, KGE and its decomposition into variability ratio (α) and bias ratio (β). Spatial comparisons using monthly WUE time series reveal moderate temporal agreement across India (median R = 0.36), with higher consistency over the Indo-Gangetic Plains, eastern India, and central agricultural regions (Fig. 12, a) where WUE variability is strongly regulated by monsoon-driven coupling between carbon uptake and water availability. Overall KGE values are low (median = 0.21) (Fig. 12, b), reflecting compounded uncertainties inherent in evaluating WUE as a ratio of two independently estimated fluxes. KGE decomposition (Fig. 12, c–d) indicates underestimation of WUE variability ($\alpha_{KGE} = 0.82$) and mean magnitude ($\beta_{KGE} = 0.85$),

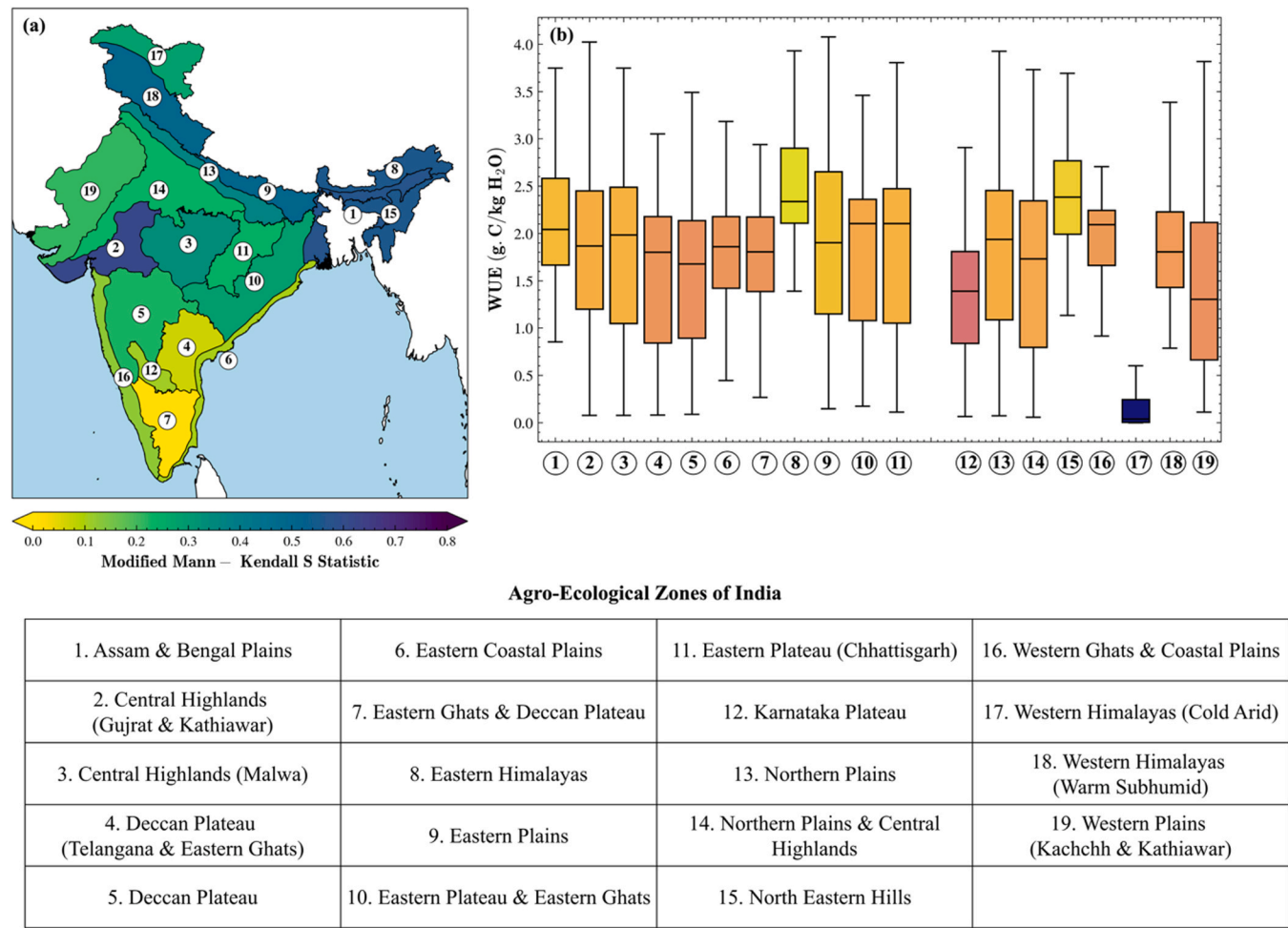


Fig. 9. (a) Modified Mann-Kendall S statistics for the period 1985–2023 over different Agro-Ecological Zones (AEZs) of India; (b) Mean Annual WUE from different Agro-Ecological zones. All the zone names corresponding to the zone numbers shown in the map are enlisted in the table.

particularly in humid and high-productivity regions of eastern and northeastern India. These biases likely arise from conservative stomatal regulation, static land-cover assumptions, and the absence of explicit irrigation, as well as known MODIS uncertainties, including biome-specific assumptions in MOD17 GPP and ET underestimation under dense canopies in MOD16. Despite these limitations, the spatial coherence of errors supports the robustness of modeled WUE patterns for diagnosing regional variability and long-term trends in the absence of direct observations.

4. Discussion

This study evaluated the model performance and extended capabilities of the Indian Land Data Assimilation System (ILDAS) in estimating GPP and ET and the resulting WUE. The current version of ILDAS is capable of simulating carbon cycle based on the vegetation scheme of Dickinson et al., (1998a),(1998b) and stomatal resistance scheme by Ball et al., (1987). In contrast, the earlier versions of ILDAS used static table LAI values for vegetation parametrizations and were primarily configured for estimating water storage variables and fluxes like soil moisture, streamflow, ET (Magotra et al., 2024a,2024b; Chakraborty et al., 2024). With this enhancement, the model is now capable of estimating carbon flux in terms of Gross Primary Production (GPP) which, when combined with ET estimates enables the evaluation of ecosystem-level WUE across the study domain.

The lower Himalayan and north-eastern hilly regions dominated by medium to dense forest cover, exhibit consistently high GPP, ET and

WUE, highlighting the strong role of forest ecosystems in sustaining productivity (Sarmah et al., 2021). Similar spatial distributions and interpretations have been supported in recent studies conducted by Dubey and Ghosh, (2023); Kumar and Sharma, (2023); Uchale et al., (2023), reinforcing our findings. Higher GPP and WUE over the lower Himalayas likely arise from an optimal coupling of high monsoon precipitation, moderate temperatures, sufficient radiation, and favorable soil moisture conditions, which together support sustained photosynthesis with relatively efficient water use.

The seasonal dynamics of GPP, ET and WUE aligns well with the findings of Verma and Ghosh, (2024), showing maximum values during the monsoon season. However, WUE peaks in the dry winter season, contrasting with their results. This difference likely stems from model structure. The Earth system models used by Verma and Ghosh, (2024) assume an instantaneous, linear GPP–WUE relationship, whereas the Ball–Berry stomatal conductance scheme in ILDAS allows a lagged physiological response that enhances water-use optimization under dry conditions—a behavior also supported by Cowan and Gd, (1977), McAdam and Brodribb, (2015) Oren et al., (1999), and recently demonstrated in Nandy et al., (2022). In fact, consistent spatial patterns can be observed in the winter maps of Fig. 4.

Recent MODIS-based studies have reported elevated WUE in arid climates, particularly during drought periods, attributing this behavior to adaptive vegetation responses under water-limited conditions and shifts in carbon–water coupling (Fathi-Taperasht et al., 2022). While some satellite remote sensing data based studies over India have reported higher WUE over the north-western arid regions attributing to

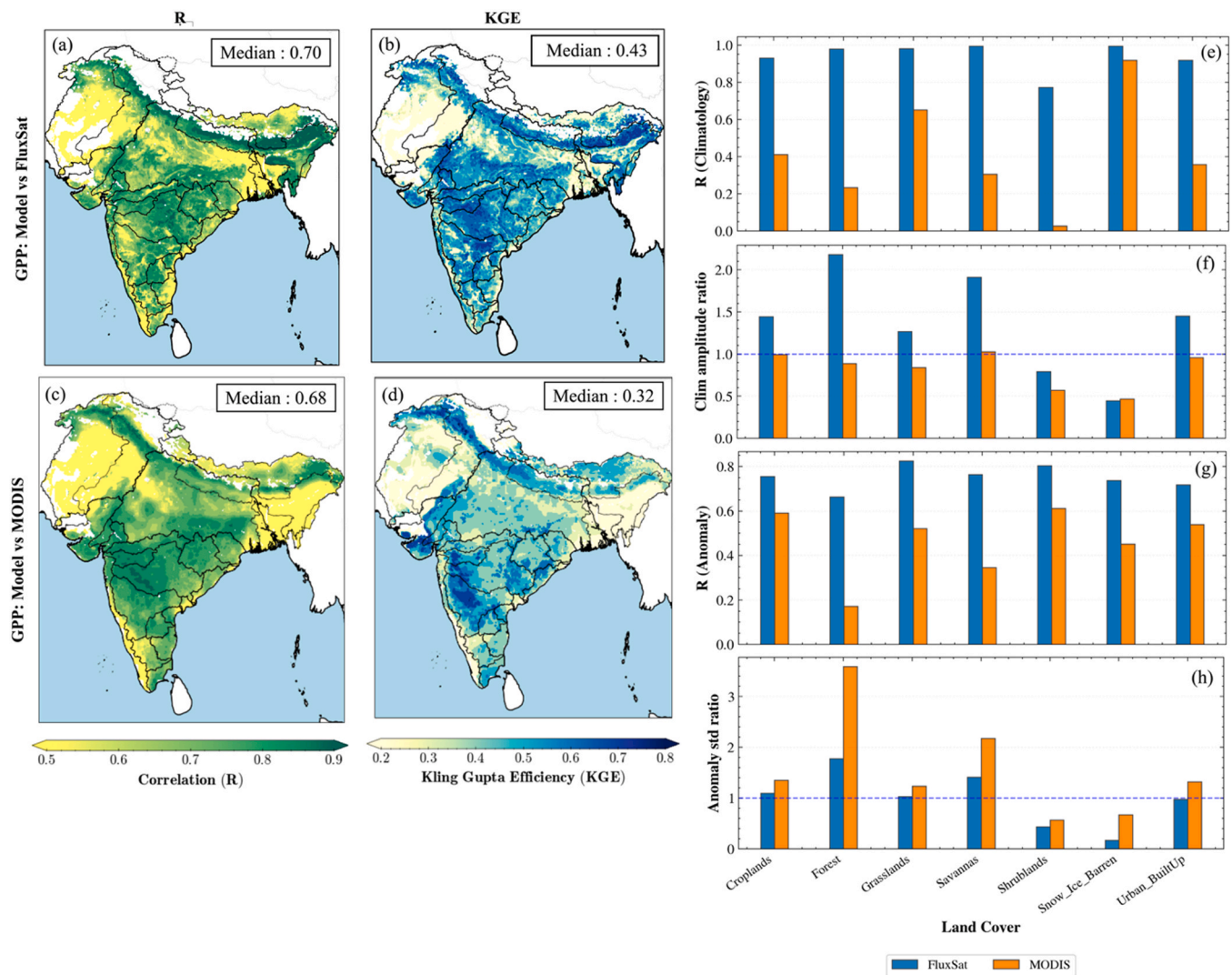


Fig. 10. Spatial evaluation of modeled GPP against FluxSat and MODIS over South Asia for 1985–2023. Panels (a–b) show Pearson correlation (R) and Kling–Gupta efficiency (KGE) between modeled GPP and FluxSat respectively, while panels (c–d) show the corresponding metrics against MODIS GPP. Panels (e–h) present land-cover-wise comparisons of climatological correlation, climatological amplitude ratio, anomaly correlation, and anomaly standard deviation ratio for major land-cover classes.

the same adaptability of vegetations to the water stress conditions (Bejagam et al., 2023; Sharma and Goyal, 2018), our model considers this region as barren land or sparsely vegetated as per the input land cover dataset (Fig. 1 and Table 2), and hence, model shows less productivity and WUE there compared to other regions throughout all the seasons, leading to less agreement with the satellite observations in the statistical analysis for those regions.

The study also reveals that Forest ecosystems dominate GPP and WUE across all seasons (Kumar and Sharma, 2023), reflecting stable canopy structure, deep rooting, and efficient carbon–water coupling, followed by savannas and croplands. Although irrigation and agricultural intensification are known to influence WUE, the present results do not show a pronounced increase in WUE over croplands, despite showing higher greening due to expansion over South Asia (Kashyap et al., 2023; Sarmah et al., 2021). This muted response likely reflects model limitations, as crop-specific growth, management practices, and irrigation are not explicitly represented. Irrigation can decouple plant water availability from precipitation, potentially increasing GPP without a proportional rise in evapotranspiration and thereby elevating WUE. Similarly, land-use changes such as increased cropping or agricultural activities may modify carbon–water interactions. Incorporating explicit irrigation schemes and dynamic land cover input represents an

important avenue for future work to better quantify agricultural influences on WUE trends.

Increasing trends of both GPP and WUE have been observed throughout the period of analysis (3.4) emphasizing the growing ecological importance of vegetation greening in South Asia (Chen et al., 2019; Kumar and Sharma, 2023; Sarmah et al., 2021). Increased atmospheric CO₂ concentrations enable vegetations to decrease evapotranspiration per unit carbon uptake by adjusting stomatal conductance (Choat et al., 2012; El Masri et al., 2019; Keenan et al., 2013b). This increase in CO₂ leads to rise in WUE from leaf (Dubey and Ghosh, 2023; Norby and Zak, 2011; Warren et al., 2011). However, higher WUE does not necessarily imply increased ecosystem resilience. In irrigated and semi-arid regions, WUE increases may partly reflect reduced transpiration driven by stomatal regulation under elevated vapor pressure deficit (VPD), rather than proportional increases in GPP, potentially weakening land–atmosphere coupling and altering local hydrology.

A key limitation of this study is the lack of direct site-level validation using eddy covariance flux tower data. Sparse availability and limited spatial coverage of long-term flux towers across South Asia restrict comprehensive ground-based validation over the South Asian region (Kumar and Sharma, 2023; Uchale et al., 2023; Verma et al., 2022), necessitating reliance on satellite and machine-learning-based products.

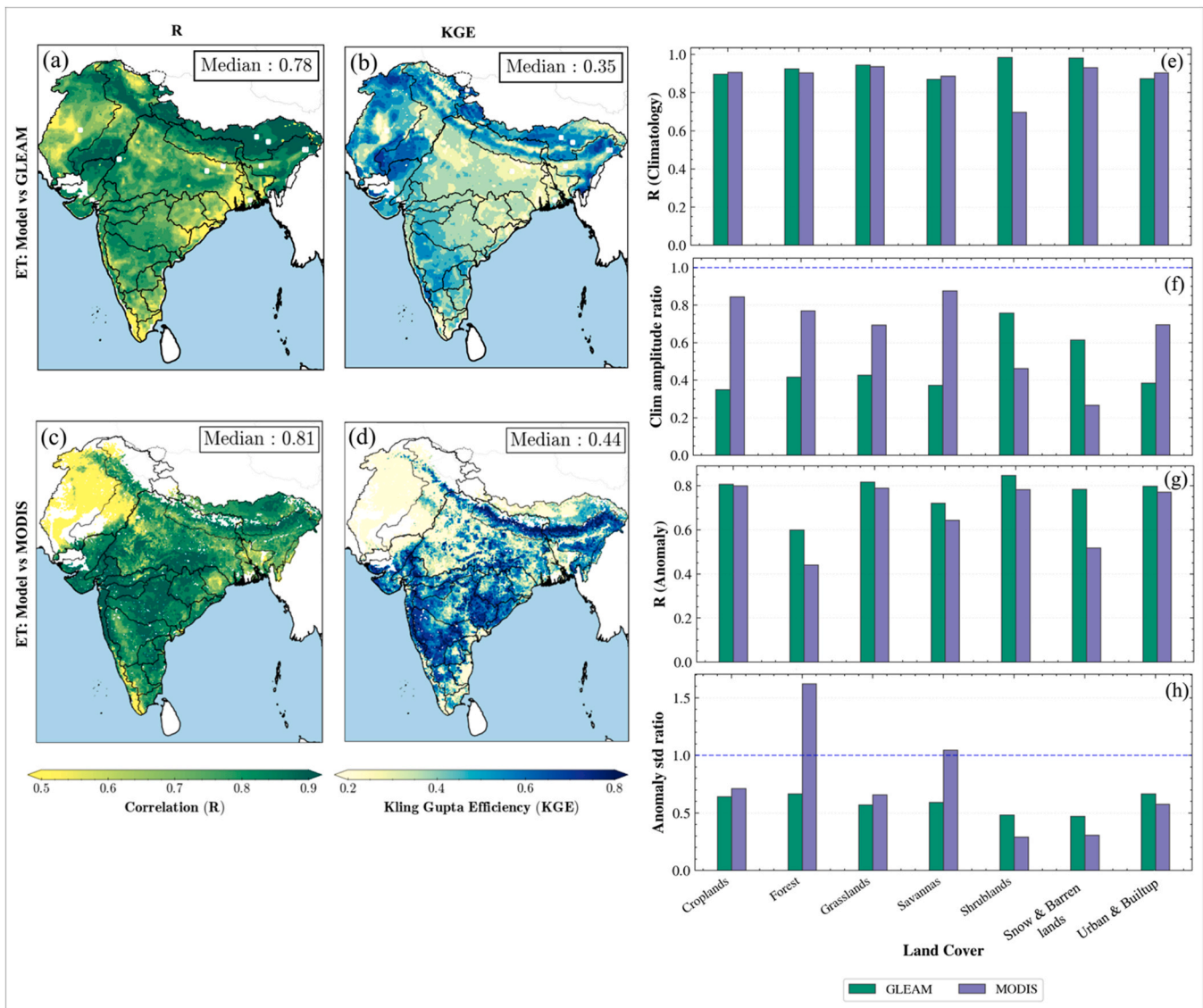


Fig. 11. Spatial evaluation of modeled ET against GLEAM and MODIS over South Asia for 1985–2023. Panels (a–b) show Pearson correlation (R) and Kling–Gupta efficiency (KGE) between modeled GPP and GLEAM, while panels (c–d) show the corresponding metrics against MODIS ET. Panels (e–h) present land-cover-wise comparisons of (e) climatological correlation, (f) climatological amplitude ratio, (g) anomaly correlation, and (h) anomaly standard deviation ratio for major land-cover classes.

FluxSat and GLEAM products are widely used for regional and global model evaluation (Ahmad et al., 2022; Bacour et al., 2019; Lv et al., 2023; Zhang et al., 2023). Although these datasets assimilate extensive flux tower observations during their development, they remain model-derived estimates rather than direct measurements. However, FluxSat being trained on flux tower dataset provides a better reliable source than MODIS GPP that has different source of uncertainties (Wang et al., 2013, 2025). Future work will leverage emerging regional flux tower networks to better constrain model uncertainties.

Although the carbon dynamics scheme in ILDA is based on well-established empirical formulations of Dickinson et al., (1998a), (1998b) and stomatal resistance scheme by Ball et al., (1987), it relies on assumptions appropriate for large-scale applications. Carbon allocation follows the default global parameterization of the dynamic vegetation scheme, with no region-specific calibration for South Asian vegetation. This ensures internal consistency and comparability with other studies but may limit representation of management-driven carbon partitioning, particularly over croplands.

Uncertainties in vegetation representation remain an important

limitation as well. The dynamic vegetation scheme uses generic MODIS land-cover classes, which do not fully capture sub-grid heterogeneity, crop diversity, management intensity, or phenological variability. These simplifications can bias simulated GPP and WUE by constraining phenological responses and carbon–water coupling in heterogeneous landscapes. These findings underscore the need for further model development, including parameter tuning, assimilation of region-specific observational datasets, and dynamic land cover integration, to improve the accuracy of ecosystem carbon–water simulations in complex landscapes. Although this study does not directly assess management interventions, the diagnosed spatiotemporal patterns of GPP and WUE provide useful guidance for water and carbon management in climate-vulnerable regions of South Asia. Identifying regions and seasons with heightened sensitivity to moisture and temperature can help inform adaptive strategies aimed at sustaining ecosystem productivity under future climate change.

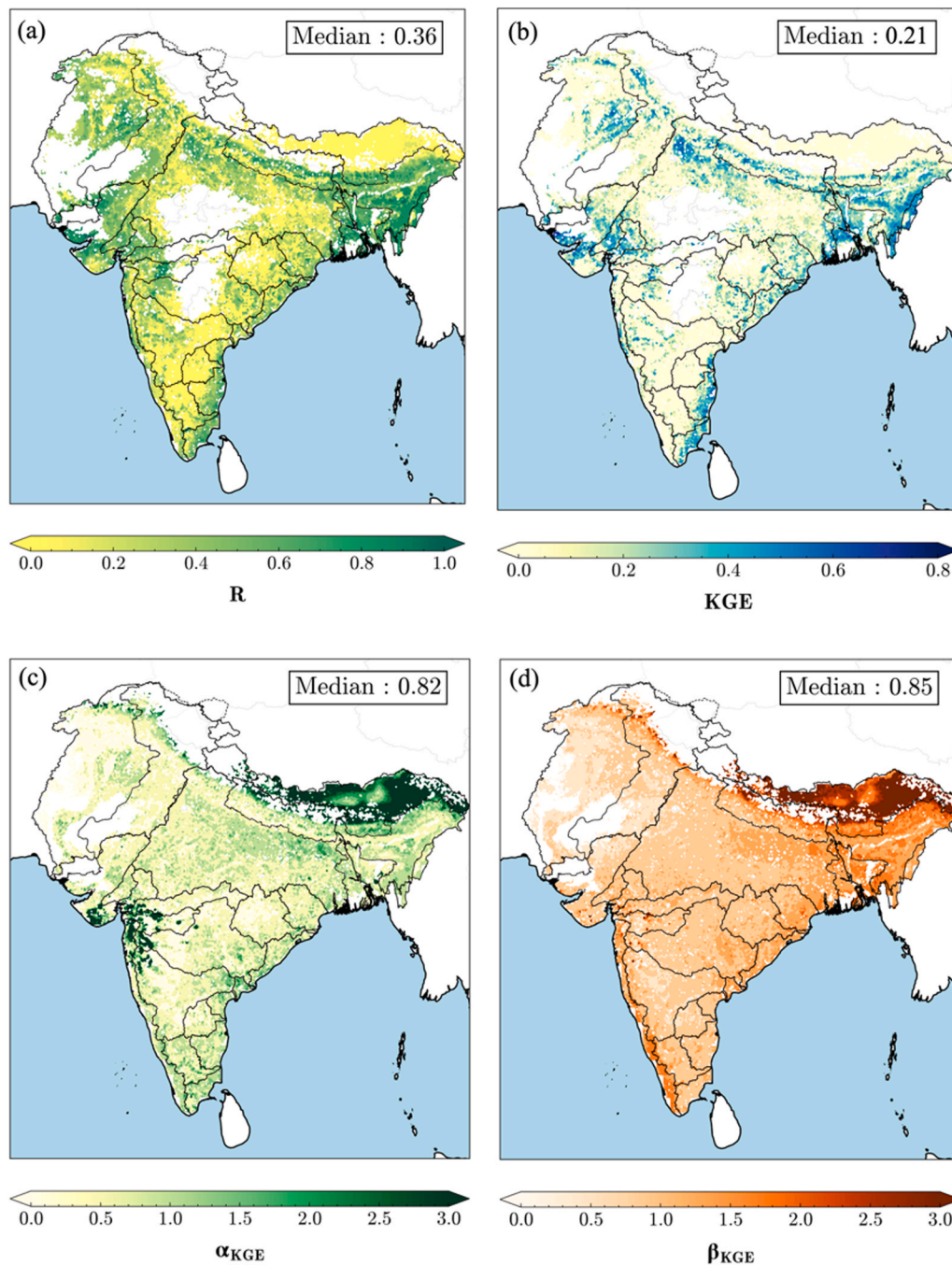


Fig. 12. Spatial patterns of model WUE performance with MODIS-derived WUE over South Asia based on (a) correlation (R), (b) KGE, and its decomposition components (c) α_{KGE} and (d) β_{KGE} .

5. Conclusions

This study integrated a dynamic vegetation scheme into the Indian Land Data Assimilation System (ILDAS) to simulate the uptake of carbon by different canopy components along with the land surface modeling framework, moving beyond static vegetation parameterizations. Model enhancements have been evaluated with other satellite and model derived datasets to analyze the spatiotemporal variation in modeled GPP and WUE along with long term trend analysis. The key conclusions from this study can be summarized as below:

- Spatial patterns show consistently high values of GPP and WUE over the lower Himalayan belt and the north-eastern portion of the

domain encompassing Ganga and Brahmaputra River basin. These regions characterized by vegetated forest and croplands underscore the critical role of forest ecosystems in regional carbon cycling.

- During the monsoon season, model estimates show high spatial variability of GPP ($\sigma = 95.44 \text{ g C/m}^2$) and ET ($\sigma = 39.60 \text{ mm}$), driven by variation in rainfall pattern and vegetation productivity. On the contrary, the pre-monsoon season exhibit relatively lower spatial variability in GPP and ET but shows high variability in WUE ($\sigma = 12.48 \text{ g C/m}^2/\text{mm}$), reflecting the complex relation between water availability and carbon assimilation during water-limited periods.
- Sensitivity analysis indicates that WUE is more sensitive to temperature and pressure out of all the meteorological forcing variables.

Whereas among the model state estimates, soil moisture and LAI are the influential drivers of WUE.

- Long term trend analysis shows statistically significant increasing trends ($p < 0.05$) for both GPP and WUE, which can be attributed to increasing vegetation greening across South Asia. Notably, the agro-ecological zones located in Northern and Central India show high values of Mann-Kendall S-statistics (>0.8), indicating significantly increasing trends of WUE.
- Statistical evaluation of model outputs against multiple satellite products in terms of correlation and KGE shows vegetated regions—particularly forests, croplands, and grasslands—as zones of high model reliability. Modeled GPP shows stronger agreement with FluxSat than with MODIS, while ET estimates exhibit higher consistency with MODIS relative to GLEAM, reflecting differences in retrieval frameworks and process representation.
- Model performance degrades in arid northwestern India and high-elevation Himalayan regions, where static land-cover assumptions (barren land, snow, and ice) suppress simulated vegetation activity, while satellite products capture episodic greening and sparse vegetation responses.
- Evaluation of WUE against MODIS-derived WUE reveals moderate temporal agreement but lower KGE, highlighting compounded uncertainties arising from ratio-based diagnostics, conservative stomatal regulation, and the absence of explicit irrigation and sub-grid land-management processes.

The observations from this study demonstrate the potentials of the updated ILDA to simulate not only hydrological but also carbon cycle variables over South Asia, offering insights into spatial variability in ecosystem WUE under changing climatic and vegetative regimes. Despite current limitations in observation-based validation and model generalizations, the framework provides a scalable tool for regional land-atmosphere interaction studies. Future improvements may involve parameter optimization, enabling a demand driven irrigation scheme, assimilation of high-resolution datasets of influential parameters, and region-specific model calibration to enhance accuracy across complex and heterogeneous landscapes.

CRediT authorship contribution statement

Manabendra Saharia: Writing – review & editing, Methodology, Conceptualization. **Arijit Chakraborty:** Writing – original draft, Methodology, Formal analysis, Data curation, Conceptualization. **Sujay V. Kumar:** Writing – review & editing. **Sumedha Chakma:** Writing – review & editing.

Compliance with ethical standards

The authors declare that they have no known competing financial interests or personal relationships that could have appeared to influence the work reported in this paper.

Declaration of Competing Interest

The authors declare that they have no known competing financial interests or personal relationships that could have appeared to influence the work reported in this paper.

Acknowledgements

This research was conducted in the HydroSense lab (<https://hydrosense.iitd.ac.in/>) of IIT Delhi and the authors acknowledge the IIT Delhi High Performance Computing facility for providing computational and storage resources. Dr. Manabendra Saharia gratefully acknowledges financial support for this work through grants from Ministry of Earth Sciences/IITM Pune Monsoon Mission III (RP04574); Ministry of Earth

Sciences (RP04741); and DST IC-IMPACTS (RP04558). Authors would like to acknowledge David M. Mocko from NASA Goddard Space Flight center for suggestions in setting up the dynamic vegetation scheme within ILDA.

Appendix A. Supporting information

Supplementary data associated with this article can be found in the online version at [doi:10.1016/j.agwat.2026.110321](https://doi.org/10.1016/j.agwat.2026.110321).

Data availability

Data will be made available on request.

References

- Ahmad, J.A., Forman, B.A., Kumar, S.V., 2022. Soil moisture estimation in South Asia via assimilation of SMAP retrievals. *Hydrol. Earth Syst. Sci.* 26 (8), 2221–2243. <https://doi.org/10.5194/hess-26-2221-2022>.
- Allen, R.G., Pereira, L.S., Howell, T.A., Jensen, M.E., 2011. Evapotranspiration information reporting: II. Recommended documentation. *Agric. Water Manag.* 98 (6), 921–929. <https://doi.org/10.1016/j.agwat.2010.12.016>.
- Anav, A., Friedlingstein, P., Beer, C., Ciais, P., Harper, A., Jones, C., Murray-Tortarolo, G., Papale, D., Parazoo, N.C., Peylin, P., Piao, S., Sitch, S., Viovy, N., Wiltshire, A., Zhao, M., 2015. Spatiotemporal patterns of terrestrial gross primary production: a review. *Rev. Geophys.* 53 (3), 785–818. <https://doi.org/10.1002/2015RG000483>.
- Arsenault, K.R., Kumar, S.V., Geiger, J.V., Wang, S., Kemp, E., Mocko, D.M., Beaudoin, H.K., Getirana, A., Navari, M., Li, B., Jacob, J., Wegiel, J., Peters-Lidard, C.D., 2018. The Land surface Data Toolkit (LDT v7.2) – a data fusion environment for land data assimilation systems. *Geosci. Model Dev.* 11 (9), 3605–3621. <https://doi.org/10.5194/gmd-11-3605-2018>.
- Bacour, C., Maignan, F., MacBean, N., Porcar-Castell, A., Flexas, J., Frankenberg, C., Peylin, P., Chevallier, F., Vuichard, N., Bastrikov, V., 2019. Improving estimates of gross primary productivity by assimilating solar-induced fluorescence satellite retrievals in a terrestrial biosphere model using a process-based SIF model. *J. Geophys. Res. Biogeosci.* 124 (11), 3281–3306. <https://doi.org/10.1029/2019JG005040>.
- Baldocchi, D., 1994. A comparative study of mass and energy exchange rates over a closed C3 (wheat) and an open C4 (corn) crop: II. CO₂ exchange and water use efficiency. *Agric. For. Meteorol.* 67 (3), 291–321. [https://doi.org/10.1016/0168-1923\(94\)90008-6](https://doi.org/10.1016/0168-1923(94)90008-6).
- Baldocchi, D., Falge, E., Gu, L., Olson, R., Hollinger, D., Running, S., Anthoni, P., Bernhofer, C., Davis, K., Evans, R., Fuentes, J., Goldstein, A., Katul, G., Law, B., Lee, X., Malhi, Y., Meyers, T., Munger, W., Oechel, W., Wofsy, S., 2001. FLUXNET: a new tool to study the temporal and spatial variability of ecosystem-scale carbon dioxide, water vapor, and energy flux densities. *Bull. Am. Meteorol. Soc.* 82 (11), 2415–2434. [https://doi.org/10.1175/1520-0477\(2001\)082<2415:FAFNTS>2.3.CO;2](https://doi.org/10.1175/1520-0477(2001)082<2415:FAFNTS>2.3.CO;2).
- Ball, J.T., Woodrow, I.E., Berry, J.A., 1987. A Model Predicting Stomatal Conductance and its Contribution to the Control of Photosynthesis under Different Environmental Conditions. In: Biggins, J. (Ed.), *Progress in Photosynthesis Research: Volume 4 Proceedings of the VIIth International Congress on Photosynthesis Providence, Rhode Island, USA, August 10–15, 1986*. Springer, Netherlands, pp. 221–224. https://doi.org/10.1007/978-94-017-0519-6_48.
- Barlage, M., Zeng, X., Wei, H., Mitchell, K.E., 2005. A global 0.05° maximum albedo dataset of snow-covered land based on MODIS observations. *Geophys. Res. Lett.* 32 (17). <https://doi.org/10.1029/2005GL022881>.
- Bejagam, V., Singh, A., Sharma, A., 2023. Spatiotemporal variability and controlling factors of ecosystem water use efficiency in India. *Theor. Appl. Climatol.* 152 (1), 813–827. <https://doi.org/10.1007/s00704-023-04418-z>.
- Bonan, B., 1996. A land surface model (LSM Version 1.0) for ecological. *Hydrol. Atmos. Stud. Tech. Descr. Use 'S. Guide*. <https://doi.org/10.5065/D6DF6P5X>.
- Boussetta, S., Balsamo, G., Beljaars, A., Kral, T., Jarlan, L., 2013. Impact of a satellite-derived leaf area index monthly climatology in a global numerical weather prediction model. *Int. J. Remote Sens.* 34 (9–10), 3520–3542. <https://doi.org/10.1080/01431161.2012.716543>.
- Campbell, J.E., Berry, J.A., Seibt, U., Smith, S.J., Montzka, S.A., Launois, T., Belviso, S., Bopp, L., Laine, M., 2017. Large historical growth in global terrestrial gross primary production. *Nature* 544 (7648), 84–87. <https://doi.org/10.1038/nature22030>.
- Chakraborty, A., Saharia, M., Chakma, S., Kumar Pandey, D., Niranjan Kumar, K., Thakur, P.K., Kumar, S., Getirana, A., 2024. Improved soil moisture estimation and detection of irrigation signal by incorporating SMAP soil moisture into the Indian Land Data Assimilation System (ILDA). *J. Hydrol.* 638, 131581. <https://doi.org/10.1016/j.jhydrol.2024.131581>.
- Chakraborty, S., Tiwari, Y.K., Deb Burman, P.K., Baidya Roy, S., Valsala, V., 2020. Observations and Modeling of GHG Concentrations and Fluxes Over India. In: Krishnan, R., Sanjay, J., Gnanaseelan, C., Mujumdar, M., Kulkarni, A., Chakraborty, S. (Eds.), *Assessment of Climate Change over the Indian Region: A Report of the Ministry of Earth Sciences (MoES), Government of India*. Springer, pp. 73–92. https://doi.org/10.1007/978-981-15-4327-2_4.

- Champion, S.H.G., Seth, S.K., 1968. A Revised Survey of the Forest Types of India. Manager of Publications.
- Chapin, F.S., Woodwell, G.M., Randerson, J.T., Rastetter, E.B., Lovett, G.M., Baldocchi, D.D., Clark, D.A., Harmon, M.E., Schimel, D.S., Valentini, R., Wirth, C., Aber, J.D., Cole, J.J., Goulden, M.L., Harden, J.W., Heimann, M., Howarth, R.W., Matson, P.A., McGuire, A.D., Schulze, E.-D., 2006. Reconciling Carbon-cycle Concepts, Terminology, and Methods. *Ecosystems* 9 (7), 1041–1050. <https://doi.org/10.1007/s10021-005-0105-7>.
- Chaudhry, P., Tambe, S., 2023. Investigation of the Indian Forest sector's performance during the last three and half decades. Article 3. *Ecol. Quest.* 34 (3). <https://doi.org/10.12775/EQ.2023.032>.
- Chen, C., Park, T., Wang, X., Piao, S., Xu, B., Chaturvedi, R.K., Fuchs, R., Brovkin, V., Ciais, P., Fensholt, R., Tømmervik, H., Bala, G., Zhu, Z., Nemani, R.R., Myneni, R.B., 2019. China and India lead in greening of the world through land-use management. *Nat. Sustain.* 2 (2), 122–129. <https://doi.org/10.1038/s41893-019-0220-7>.
- Cheng, L., Zhang, L., Wang, Y.-P., Canadell, J.G., Chiew, F.H.S., Beringer, J., Li, L., Miralles, D.G., Piao, S., Zhang, Y., 2017. Recent increases in terrestrial carbon uptake at little cost to the water cycle. *Nat. Commun.* 8 (1), 110. <https://doi.org/10.1038/s41467-017-00114-5>.
- Choat, B., Jansen, S., Brodribb, T.J., Cochard, H., Delzon, S., Bhaskar, R., Bucci, S.J., Feild, T.S., Gleason, S.M., Hacke, U.G., Jacobsen, A.L., Lens, F., Maherali, H., Martínez-Vilalta, J., Mayr, S., Mencuccini, M., Mitchell, P.J., Nardini, A., Pittermann, J., Zanne, A.E., 2012. Global convergence in the vulnerability of forests to drought. *Nature* 491 (7426), 752–755. <https://doi.org/10.1038/nature11688>.
- Collalti, A., Prentice, I.C., 2019. Is NPP proportional to GPP? Waring's hypothesis 20 years on. *Tree Physiol.* 39 (8), 1473–1483. <https://doi.org/10.1093/treephys/tpz034>.
- Collatz, G.J., Ball, J.T., Grivet, C., Berry, J.A., 1991. Physiological and environmental regulation of stomatal conductance, photosynthesis and transpiration: A model that includes a laminar boundary layer. *Agros. For. Meteorol.* 54 (2), 107–136. [https://doi.org/10.1016/0168-1923\(91\)90002-8](https://doi.org/10.1016/0168-1923(91)90002-8).
- Cowan, I., Gd, F., 1977. STOMATAL FUNCTION IN RELATION TO LEAF METABOLISM AND ENVIRONMENT. *STOMATAL Funct. Relat. LEAF Metab. Environ.*
- Dai, Y., Zeng, X., Dickinson, R.E., Baker, I., Bonan, G.B., Bosilovich, M.G., Denning, A.S., Dirmeyer, P.A., Houser, P.R., Niu, G., Oleson, K.W., Schlosser, C.A., Yang, Z.-L., 2003. The Common Land Model. *Bull. Am. Meteorol. Soc.* 84 (8), 1013–1024. <https://doi.org/10.1175/BAMS-84-8-1013>.
- Das, R., Chaturvedi, R.K., Roy, A., Karmakar, S., Ghosh, S., 2023. Warming inhibits increases in vegetation net primary productivity despite greening in India. *Sci. Rep.* 13 (1), 21309. <https://doi.org/10.1038/s41598-023-48614-3>.
- Deb Burman, P.K., Sarma, D., Williams, M., Karipot, A., Chakraborty, S., 2017. Estimating gross primary productivity of a tropical forest ecosystem over north-east India using LAI and meteorological variables. *J. Earth Syst. Sci.* 126 (7), 99. <https://doi.org/10.1007/s12040-017-0874-3>.
- Dickinson, R.E., 1983. Land Surface Processes and Climate—Surface Albedos and Energy Balance. In: *In: Saltzman, B. (Ed.), Advances in Geophysics*, 25. Elsevier, pp. 305–353. [https://doi.org/10.1016/S0065-2687\(08\)60176-4](https://doi.org/10.1016/S0065-2687(08)60176-4).
- Dickinson, R.E., Shaikh, M., Bryant, R., Graumlich, L., 1998a. Interactive Canopies for a Climate Model. *J. Clim.* 11 (11), 2823–2836.
- Dickinson, R.E., Shaikh, M., Bryant, R., Graumlich, L., 1998b. Interactive Canopies for a Climate Model. *J. Clim.* 11 (11), 2823–2836.
- Dubey, N., Ghosh, S., 2023. CO₂ fertilization enhances vegetation productivity and reduces ecological drought in India. *Environ. Res. Lett.* 18 (6), 064025. <https://doi.org/10.1088/1748-9326/acd5e7>.
- Ek, M.B., Mitchell, K.E., Lin, Y., Rogers, E., Grunmann, P., Koren, V., Gayno, G., Tarpley, J.D., 2003. Implementation of Noah land surface model advances in the National Centers for Environmental Prediction operational mesoscale Eta model. *J. Geophys. Res. Atmospheres* 108 (D22). <https://doi.org/10.1029/2002JD003296>.
- El Masri, B., Schwalm, C., Huntzinger, D.N., Mao, J., Shi, X., Peng, C., Fisher, J.B., Jain, A.K., Tian, H., Poulter, B., Michalak, A.M., 2019. Carbon and Water Use Efficiencies: A Comparative Analysis of Ten Terrestrial Ecosystem Models under Changing Climate. *Sci. Rep.* 9 (1), 14680. <https://doi.org/10.1038/s41598-019-50808-7>.
- Farquhar, G.D., von Caemmerer, S., Berry, J.A., 1980. A biochemical model of photosynthetic CO₂ assimilation in leaves of C₃ species. *Planta* 149 (1), 78–90. <https://doi.org/10.1007/BF00386231>.
- Fathi-Taperasht, A., Shafizadeh-Moghadam, H., Kouchakzadeh, M., 2022. MODIS-based evaluation of agricultural drought, water use efficiency and post-drought in Iran; considering the influence of heterogeneous climatic regions. *J. Clean. Prod.* 374, 133836. <https://doi.org/10.1016/j.jclepro.2022.133836>.
- Frankenberg, C., Fisher, J.B., Worden, J., Badgley, G., Saatchi, S.S., Lee, J.-E., Toon, G.C., Butz, A., Jung, M., Kuze, A., Yokota, T., 2011. New global observations of the terrestrial carbon cycle from GOSAT: Patterns of plant fluorescence with gross primary productivity. *Geophys. Res. Lett.* 38 (17). <https://doi.org/10.1029/2011GL048738>.
- Friedl, M.A., McIver, D.K., Hodges, J.C.F., Zhang, X.Y., Muchoney, D., Strahler, A.H., Woodcock, C.E., Gopal, S., Schneider, A., Cooper, A., Baccini, A., Gao, F., Schaaf, C., 2002. Global land cover mapping from MODIS: Algorithms and early results. *Remote Sens. Environ. Moderat. Resolut. Imaging Spectroradiometer (MODIS) A N. Gener. Land Surf. Monit.* 83 (1), 287–302. [https://doi.org/10.1016/S0034-4257\(02\)00078-0](https://doi.org/10.1016/S0034-4257(02)00078-0).
- Fu, Z., Ciais, P., Wigneron, J.-P., Gentile, P., Feldman, A.F., Makowski, D., Viovy, N., Kemanian, A.R., Goll, D.S., Stoy, P.C., Prentice, I.C., Yakir, D., Liu, L., Ma, H., Li, Xiaojun, Huang, Y., Yu, K., Zhu, P., Li, Xing, Smith, W.K., 2024. Global critical soil moisture thresholds of plant water stress. *Nat. Commun.* 15 (1), 4826. <https://doi.org/10.1038/s41467-024-49244-7>.
- G, B., Sharma, G., R, S.S.J., 2022. Forest cover in India: A victim of technicalities. *Ecol. Econ.* 193, 107306. <https://doi.org/10.1016/j.ecolecon.2021.107306>.
- Gelaro, R., McCarty, W., Suárez, M.J., Todling, R., Molod, A., Takacs, L., Randles, C.A., Darmenov, A., Bosilovich, M.G., Reichle, R., Wargan, K., Coy, L., Cullather, R., Draper, C., Akella, S., Buchard, V., Conaty, A., Silva, A.M. da, Gu, W., Zhao, B., 2017. The Modern-Era Retrospective Analysis for Research and Applications, Version 2 (MERRA-2). *J. Clim.* 30 (14), 5419–5454. <https://doi.org/10.1175/JCLI-D-16-0758.1>.
- Green, J.K., Seneviratne, S.I., Berg, A.M., Findell, K.L., Hagemann, S., Lawrence, D.M., Gentile, P., 2019. Large influence of soil moisture on long-term terrestrial carbon uptake. Article 7740. *Nature* 565 (7740). <https://doi.org/10.1038/s41586-018-0848-x>.
- Greve, P., Roderick, M.L., Seneviratne, S.I., 2017. Simulated changes in aridity from the last glacial maximum to 4xCO₂. *Environ. Res. Lett.* 12 (11), 114021. <https://doi.org/10.1088/1748-9326/aa89a3>.
- Gupta, H.V., Kling, H., 2011. On typical range, sensitivity, and normalization of Mean Squared Error and Nash-Sutcliffe Efficiency type metrics. *Water Resour. Res.* 47 (10). <https://doi.org/10.1029/2011WR010962>.
- Gutman, G., Ignatov, A., 1998. The derivation of the green vegetation fraction from NOAA/AVHRR data for use in numerical weather prediction models. *Int. J. Remote Sens.* 19 (8), 1533–1543. <https://doi.org/10.1080/014311698215333>.
- Hamed, K.H., Ramachandra Rao, A., 1998. A modified Mann-Kendall trend test for autocorrelated data. *J. Hydrol.* 204 (1), 182–196. [https://doi.org/10.1016/S0022-1694\(97\)00125-X](https://doi.org/10.1016/S0022-1694(97)00125-X).
- He, C., Chen, F., Barlage, M., Yang, Z.-L., Wegiel, J.W., Niu, G.-Y., Gochis, D., Mocko, D. M., Abolafia-Rosenzweig, R., Zhang, Z., Lin, T.-S., Valayamkunnath, P., Ek, M., Niyogi, D., 2023. Enhancing the Community Noah-MP Land Model Capabilities for Earth Sciences and Applications. *Bull. Am. Meteorol. Soc.* 104 (11), E2023-E2029. <https://doi.org/10.1175/BAMS-D-23-0249.1>.
- Hosseini, A., Mocko, D.M., Brunzell, N.A., Kumar, S.V., Mahanama, S., Arsenault, K., Roundy, J.K., 2022. Understanding the impact of vegetation dynamics on the water cycle in the Noah-MP model. *Front. Water* 4. <https://doi.org/10.3389/frwa.2022.925852>.
- Huang, M., Piao, S., Sun, Y., Ciais, P., Cheng, L., Mao, J., Poulter, B., Shi, X., Zeng, Z., Wang, Y., 2015. Change in terrestrial ecosystem water-use efficiency over the last three decades. *Glob. Change Biol.* 21 (6), 2366–2378. <https://doi.org/10.1111/gcb.12873>.
- Huxman, T.E., Smith, M.D., Fay, P.A., Knapp, A.K., Shaw, M.R., Loik, M.E., Smith, S.D., Tissue, D.T., Zak, J.C., Weltzin, J.F., Pockman, W.T., Sala, O.E., Haddad, B.M., Harte, J., Koch, G.W., Schwinning, S., Small, E.E., Williams, D.G., 2004. Convergence across biomes to a common rain-use efficiency. *Nature* 429 (6992), 651–654. <https://doi.org/10.1038/nature02561>.
- Ito, A., Inatomi, M., 2012. Water-Use Efficiency of the Terrestrial Biosphere: A Model Analysis Focusing on Interactions between the Global Carbon and Water Cycles. *J. Hydrometeorol.* 13 (2), 681–694. <https://doi.org/10.1175/JHM-D-10-05034.1>.
- Joiner, J., Yoshida, Y., 2020. Satellite-based reflectances capture large fraction of variability in global gross primary production (GPP) at weekly time scales. *Agric. For. Meteorol.* 291, 108092. <https://doi.org/10.1016/j.agrformet.2020.108092>.
- Justice, C.O., Townshend, J.R.G., Vermote, E.F., Masuoka, E., Wolfe, R.E., Saleous, N., Roy, D.P., Morisette, J.T., 2002. An overview of MODIS Land data processing and product status. *Remote Sens. Environ. Moderat. Resolut. Imaging Spectroradiometer (MODIS) A N. Gener. Land Surf. Monit.* 83 (1), 3–15. [https://doi.org/10.1016/S0034-4257\(02\)00084-6](https://doi.org/10.1016/S0034-4257(02)00084-6).
- Kashyap, R., Kuttippurath, J., Kumar, P., 2023. Browning of vegetation in efficient carbon sink regions of India during the past two decades is driven by climate change and anthropogenic intrusions. *J. Environ. Manag.* 336, 117655. <https://doi.org/10.1016/j.jenvman.2023.117655>.
- Keenan, T.F., Hollinger, D.Y., Bohrer, G., Dragoni, D., Munger, J.W., Schmid, H.P., Richardson, A.D., 2013b. Increase in forest water-use efficiency as atmospheric carbon dioxide concentrations rise. *Nature* 499 (7458), 324–327. <https://doi.org/10.1038/nature12291>.
- Keenan, T.F., Hollinger, D.Y., Bohrer, G., Dragoni, D., Munger, J.W., Schmid, H.P., Richardson, A.D., 2013a. Increase in forest water-use efficiency as atmospheric carbon dioxide concentrations rise. *Nature* 499 (7458), 324–327. <https://doi.org/10.1038/nature12291>.
- Kim, H., Wigneron, J.-P., Kumar, S., Dong, J., Wagner, W., Cosh, M.H., Bosch, D.D., Collins, C.H., Starks, P.J., Seyfried, M., Lakshmi, V., 2020. Global scale error assessments of soil moisture estimates from microwave-based active and passive satellites and land surface models over forest and mixed irrigated/dryland agriculture regions. *Remote Sens. Environ.* 251, 112052. <https://doi.org/10.1016/j.rse.2020.112052>.
- Konapala, G., Mishra, A.K., 2016. Three-parameter-based streamflow elasticity model: Application to MOPEX basins in the USA at annual and seasonal scales. *Hydrol. Earth Syst. Sci.* 20 (6), 2545–2556. <https://doi.org/10.5194/hess-20-2545-2016>.
- Koster, R.D., Suarez, M.J., Ducharme, A., Stieglitz, M., Kumar, P., 2000. A catchment-based approach to modeling land surface processes in a general circulation model: 1. Model structure. *J. Geophys. Res. Atmospheres* 105 (D20), 24809–24822. <https://doi.org/10.1029/2000JD900327>.
- Kumar, S.V., Peters-Lidard, C.D., Tian, Y., Houser, P.R., Geiger, J., Olden, S., Lighty, L., Eastman, J.L., Doty, B., Dirmeyer, P., Adams, J., Mitchell, K., Wood, E.F., Sheffield, J., 2006. Land information system: An interoperable framework for high resolution land surface modeling. *Environ. Model. & Softw.* 21 (10), 1402–1415. <https://doi.org/10.1016/j.envsoft.2005.07.004>.
- Kumar, S.V., Reichle, R.H., Peters-Lidard, C.D., Koster, R.D., Zhan, X., Crow, W.T., Eylander, J.B., Houser, P.R., 2008. A land surface data assimilation framework using the land information system: Description and applications. *Adv. Water Resour.*

- Hydrol. Remote Sens. 31 (11), 1419–1432. <https://doi.org/10.1016/j.advwatres.2008.01.013>.
- Kumar, S., Sharma, L.K., 2023. Assessment of water and carbon use efficiency in the SAARC region for ecological resilience under changing climate. *J. Environ. Manag.* 326, 116812. <https://doi.org/10.1016/j.jenvman.2022.116812>.
- Laanaia, N., Carrer, D., Calvet, J.-C., Pagé, C., 2016. How will climate change affect the vegetation cycle over France? A generic modeling approach. *Clim. Risk Manag.* 13, 31–42. <https://doi.org/10.1016/j.crm.2016.06.001>.
- Li, X., Xiao, J., He, B., 2018. Chlorophyll fluorescence observed by OCO-2 is strongly related to gross primary productivity estimated from flux towers in temperate forests. *Remote Sens. Environ.* 204, 659–671. <https://doi.org/10.1016/j.rse.2017.09.034>.
- Li, Y., Xie, X., Yuan, W., 2025. Increased atmospheric water demand reduces ecosystem water use efficiency. *J. Hydrol.* 656, 133031. <https://doi.org/10.1016/j.jhydrol.2025.133031>.
- Lin, Y., Grace, J., Zhao, W., Dong, Y., Zhang, X., Zhou, L., Fei, X., Jin, Y., Li, J., Nizami, S. M., Balasubramanian, D., Zhou, W., Liu, Y., Song, Q., Sha, L., Zhang, Y., 2018. Water-use efficiency and its relationship with environmental and biological factors in a rubber plantation. *J. Hydrol.* 563, 273–282. <https://doi.org/10.1016/j.jhydrol.2018.05.026>.
- Liu, D., Mishra, A.K., Ray, D.K., 2020. Sensitivity of global major crop yields to climate variables: a non-parametric elasticity analysis. *Sci. Total Environ.* 748, 141431. <https://doi.org/10.1016/j.scitotenv.2020.141431>.
- Liu, D., Mishra, A.K., Zhang, K., 2017. Runoff sensitivity over Asia: role of climate variables and initial soil conditions. *J. Geophys. Res. Atmos.* 122 (4), 2218–2238. <https://doi.org/10.1002/2016JD025694>.
- Loew, A., Stacke, T., Dorigo, W., de Jeu, R., Hagemann, S., 2013. Potential and limitations of multidecadal satellite soil moisture observations for selected climate model evaluation studies. *Hydrol. Earth Syst. Sci.* 17 (9), 3523–3542. <https://doi.org/10.5194/hess-17-3523-2013>.
- Lv, Y., Liu, J., He, W., Zhou, Y., Tu Nguyen, N., Bi, W., Wei, X., Chen, H., 2023. How well do light-use efficiency models capture large-scale drought impacts on vegetation productivity compared with data-driven estimates? *Ecol. Indic.* 146, 109739. <https://doi.org/10.1016/j.ecolind.2022.109739>.
- Madani, N., Kimball, J.S., Running, S.W., 2017. Improving global gross primary productivity estimates by computing optimum light use efficiencies using flux tower data. *J. Geophys. Res. Biogeosci.* 122 (11), 2939–2951. <https://doi.org/10.1002/2017JG004142>.
- Magotra, B., Prakash, V., Saharia, M., Getirana, A., Kumar, S., Pradhan, R., Dhanya, C.T., Rajagopalan, B., Singh, R.P., Pandey, A., Mohapatra, M., 2024a. Towards an Indian land data assimilation system (ILDAS): A coupled hydrologic-hydraulic system for water balance assessments. *J. Hydrol.* 629, 130604. <https://doi.org/10.1016/j.jhydrol.2023.130604>.
- Magotra, B., Prakash, V., Saharia, M., Getirana, A., Kumar, S., Pradhan, R., Dhanya, C.T., Rajagopalan, B., Singh, R.P., Pandey, A., Mohapatra, M., 2024b. Towards an Indian land data assimilation system (ILDAS): a coupled hydrologic-hydraulic system for water balance assessments. *J. Hydrol.* 629, 130604. <https://doi.org/10.1016/j.jhydrol.2023.130604>.
- Mann, H.B., 1945. Nonparametric tests against trend. *Econometrica* 13 (3), 245–259. <https://doi.org/10.2307/1907187>.
- McAdam, S.A.M., Brodribb, T.J., 2015. The evolution of mechanisms driving the stomatal response to vapor pressure deficit. *Plant Physiol.* 167 (3), 833–843. <https://doi.org/10.1104/pp.114.252940>.
- Mengoli, G., Agustí-Panareda, A., Boussetta, S., Harrison, S.P., Trotta, C., Prentice, I.C., 2022. Ecosystem photosynthesis in land-surface models: a first-principles approach incorporating acclimation. *J. Adv. Model. Earth Syst.* 14 (1), e2021MS002767. <https://doi.org/10.1029/2021MS002767>.
- Miralles, D.G., Holmes, T.R.H., De Jeu, R. a. M., Gash, J.H., Meesters, A.G.C.A., Dolman, A.J., 2011. Global land-surface evaporation estimated from satellite-based observations. *Hydrol. Earth Syst. Sci.* 15 (2), 453–469. <https://doi.org/10.5194/hess-15-453-2011>.
- Nandy, S., Saranya, M., Srinet, R., 2022. Spatio-temporal variability of water use efficiency and its drivers in major forest formations in India. *Remote Sens. Environ.* 269, 112791. <https://doi.org/10.1016/j.rse.2021.112791>.
- Nie, W., Zaitchik, B.F., Rodell, M., Kumar, S.V., Anderson, M.C., Hain, C., 2018. Groundwater withdrawals under drought: reconciling GRACE and land surface models in the United States high plains aquifer. *Water Resour. Res.* 54 (8), 5282–5299. <https://doi.org/10.1029/2017WR022178>.
- Niu, S., Xing, X., Zhang, Z., Xia, J., Zhou, X., Song, B., Li, L., Wan, S., 2011. Water-use efficiency in response to climate change: from leaf to ecosystem in a temperate steppe. *Glob. Change Biol.* 17 (2), 1073–1082. <https://doi.org/10.1111/j.1365-2486.2010.02280.x>.
- Norby, R.J., Zak, D.R., 2011. Ecological Lessons from Free-Air CO₂ Enrichment (FACE) Experiments. *Annu. Rev. Ecol. Evol. Syst.* 42 (4), 181–203. <https://doi.org/10.1146/annurev-ecolsys-102209-144647>.
- Oren, R., Sperry, J.S., Katul, G.G., Pataki, D.E., Ewers, B.E., Phillips, N., Schäfer, K.V.R., 1999. Survey and synthesis of intra- and interspecific variation in stomatal sensitivity to vapour pressure deficit. *Plant Cell Environ.* 22 (12), 1515–1526. <https://doi.org/10.1046/j.1365-3040.1999.00513.x>.
- Pai, D., Sridhar, L., Rajeevan, M., Sreejith, O., Satbhai, N.S., & Mukhopadhyay, B. (2014). *Development of a new high spatial resolution (0.25° × 0.25°) long period (1901–2010) daily gridded rainfall data set over India and its comparison with existing data sets over the region.* ([https://www.semanticscholar.org/paper/Development-of-a-new-high-spatial-resolution-\(0.25%C2%B0-Pai-Sridhar/f24d17a376ec4d104024840c33092b5334bc3740\)](https://www.semanticscholar.org/paper/Development-of-a-new-high-spatial-resolution-(0.25%C2%B0-Pai-Sridhar/f24d17a376ec4d104024840c33092b5334bc3740))).
- Peddinti, S.R., Kambhammettu, B.V.N.P., Rodda, S.R., Thumaty, K.C., Suradhaniwar, S., 2020. Dynamics of ecosystem water use efficiency in citrus orchards of central india using eddy covariance and landsat measurements. *Ecosystems* 23 (3), 511–528. <https://doi.org/10.1007/s10021-019-00416-3>.
- Peters-Lidard, C.D., Houser, P.R., Tian, Y., Kumar, S.V., Geiger, J., Olden, S., Lighty, L., Doty, B., Dirmeyer, P., Adams, J., Mitchell, K., Wood, E.F., Sheffield, J., 2007. High-performance earth system modeling with NASA/GSFC's land information system. *Innov. Syst. Softw. Eng.* 3 (3), 157–165. <https://doi.org/10.1007/s11334-007-0028-x>.
- Qiu, R., Katul, G.G., Zhang, L., Qin, S., Jiang, X., 2025. The effects of changing environments, abiotic stresses, and management practices on cropland evapotranspiration: a review. *Rev. Geophys.* 63 (1), e2024RG000858. <https://doi.org/10.1029/2024RG000858>.
- Reichstein, M., Falge, E., Baldocchi, D., Papale, D., Aubinet, M., Berbigier, P., Bernhofer, C., Buchmann, N., Gilmanov, T., Granier, A., Grünwald, T., Havránková, K., Ilvesniemi, H., Janous, D., Knohl, A., Laurila, T., Lohila, A., Loustau, D., Matteucci, G., Valentini, R., 2005. On the separation of net ecosystem exchange into assimilation and ecosystem respiration: review and improved algorithm. *Glob. Change Biol.* 11 (9), 1424–1439. <https://doi.org/10.1111/j.1365-2486.2005.001002.x>.
- Robinson, D.A., & Kukla, G. (1985). *Maximum Surface Albedo of Seasonally Snow-Covered Lands in the Northern Hemisphere.* (https://journals.ametsoc.org/view/journals/apm/24/5/1520-0450.1985.024.0402_msaoss.2.0.co_2.xml).
- Roderick, M.L., Greve, P., Farquhar, G.D., 2015. On the assessment of aridity with changes in atmospheric CO₂. *Water Resour. Res.* 51 (7), 5450–5463. <https://doi.org/10.1002/2015WR017031>.
- Running, S., Mu, Q., & Zhao, M. (2021). *MODIS/Terra Net Evapotranspiration 8-Day L4 Global 500m SIN Grid V061* | NASA Earthdata [Dataset]. Earth Science Data Systems, NASA. (<https://www.earthdata.nasa.gov/data/catalog/lpcloud-mod16a2-061>).
- Running, S.W., Nemani, R.R., Heinsch, F.A., Zhao, M., Reeves, M., Hashimoto, H., 2004. A Continuous Satellite-Derived Measure of Global Terrestrial Primary Production. *BioScience* 54 (6), 547–560. [https://doi.org/10.1641/0006-3568\(2004\)054\[0547:ACSMOG\]2.0.CO;2](https://doi.org/10.1641/0006-3568(2004)054[0547:ACSMOG]2.0.CO;2).
- Running, S.W., & Zhao, M. (2021). *Daily GPP and Annual NPP (MOD17A2H/A3H) and Year-end Gap-Filled (MOD17A2HGF/A3HGF) Products NASA Earth Observing System MODIS Land Algorithm (For Collection 6.1).* (<https://www.umd.edu/numerical-terradynamic-simulation-group/project/modis/user-guides/mod17c61usersguidev11mar112021.pdf>).
- Sarmah, S., Singha, M., Wang, J., Dong, J., Deb Burman, P.K., Goswami, S., Ge, Y., Ilyas, S., Niu, S., 2021. Mismatches between vegetation greening and primary productivity trends in South Asia – A satellite evidence. *Int. J. Appl. Earth Obs. Geoinf.* 104, 102561. <https://doi.org/10.1016/j.jag.2021.102561>.
- Schaake, J., & Waggoner, P. (1990). *From climate to flow.* (<https://www.semanticscholar.org/paper/From-climate-to-flow-Schaake-Waggoner/5859309f2abf316fa939c1d0f14837e80c69c091>).
- Sellers, P.J., 1985. Canopy reflectance, photosynthesis and transpiration. *Int. J. Remote Sens.* 6 (8), 1335–1372. <https://doi.org/10.1080/01431168508948283>.
- Sen, P.K., 1968. Estimates of the Regression Coefficient Based on Kendall's Tau. *J. Am. Stat. Assoc.* 63 (324), 1379–1389. <https://doi.org/10.1080/01621459.1968.10480934>.
- Sharma, A., Goyal, M.K., 2018. District-level assessment of the ecohydrological resilience to hydroclimatic disturbances and its controlling factors in India. *J. Hydrol.* 564, 1048–1057. <https://doi.org/10.1016/j.jhydrol.2018.07.079>.
- Shepard, D., 1968. A two-dimensional interpolation function for irregularly-spaced data. *Proceedings of the 1968 23rd ACM National Conference On. The 1968 23rd ACM national conference*, pp. 517–524. <https://doi.org/10.1145/800186.810616>.
- Sun, H., Bai, Y., Lu, M., Wang, J., Tuo, Y., Yan, D., Zhang, W., 2021. Drivers of the water use efficiency changes in China during 1982–2015. *Sci. Total Environ.* 799, 149145. <https://doi.org/10.1016/j.scitotenv.2021.149145>.
- Tang, X., Li, H., Desai, A.R., Nagy, Z., Luo, J., Kolb, T.E., Olioso, A., Xu, X., Yao, L., Kutsch, W., Pilegaard, K., Köstner, B., Ammann, C., 2014. How is water-use efficiency of terrestrial ecosystems distributed and changing on Earth? *Sci. Rep.* 4 (1), 7483. <https://doi.org/10.1038/srep07483>.
- Tang, X., Li, H., Xu, X., Luo, J., Li, X., Ding, Z., Xie, J., 2016. Potential of MODIS data to track the variability in ecosystem water-use efficiency of temperate deciduous forests. *Ecol. Eng.* 91, 381–391. <https://doi.org/10.1016/j.ecoleng.2016.02.022>.
- Tesfaye, S., Taye, G., Birhane, E., van der Zee, S.E.A.T.M., 2021. Spatiotemporal variability of ecosystem water use efficiency in northern Ethiopia during 1982–2014. *J. Hydrol.* 603, 126863. <https://doi.org/10.1016/j.jhydrol.2021.126863>.
- Tian, H., Chen, G., Liu, M., Zhang, C., Sun, G., Lu, C., Xu, X., Ren, W., Pan, S., Chappellka, A., 2010. Model estimates of net primary productivity, evapotranspiration, and water use efficiency in the terrestrial ecosystems of the southern United States during 1895–2007. *For. Ecol. Manag. Manag. Landsc. Mult. Scales Sustain. Ecosyst. Funct.* 259 (7), 1311–1327. <https://doi.org/10.1016/j.foreco.2009.10.009>.
- Uchale, G., Burman, P.K.D., Tiwari, Y.K., Datye, A., Sarkar, A., 2023. Investigating terrestrial carbon uptake over India using multimodel simulations of gross primary productivity and satellite-based biophysical product. *J. Geophys. Res. Biogeosci.* 128 (11), e2023JG007468. <https://doi.org/10.1029/2023JG007468>.
- Veettil, A.V., Konapala, G., Mishra, A.K., Li, H.-Y., 2018. Sensitivity of drought resilience-vulnerability- exposure to hydrologic ratios in contiguous United States. *J. Hydrol.* 564, 294–306. <https://doi.org/10.1016/j.jhydrol.2018.07.015>.
- Verma, A., Chandel, V., Ghosh, S., 2022. Climate drivers of the variations of vegetation productivity in India. *Environ. Res. Lett.* 17 (8), 084023. <https://doi.org/10.1088/1748-9326/ac7c7f>.

- Verma, A., Ghosh, S., 2024. Unveiling the role of past vapor pressure deficit through soil moisture in driving tropical vegetation productivity. *Environ. Res. Lett.* 19 (10), 104040. <https://doi.org/10.1088/1748-9326/ad7520>.
- Wang, K., Dickinson, R.E., 2012. A review of global terrestrial evapotranspiration: Observation, modeling, climatology, and climatic variability. *Rev. Geophys.* 50 (2). <https://doi.org/10.1029/2011RG000373>.
- Wang, X., Ma, M., Li, X., Song, Y., Tan, J., Huang, G., Zhang, Z., Zhao, T., Feng, J., Ma, Z., Wei, W., Bai, Y., 2013. Validation of MODIS-GPP product at 10 flux sites in northern China. *Int. J. Remote Sens.* 34 (2), 587–599. <https://doi.org/10.1080/01431161.2012.715774>.
- Wang, Y., She, X., Zhu, C., Chen, J., Kong, D., Shi, W., Guan, X., Xie, Q., Gao, X., Li, W., Li, Y., 2025. Unveiling the accuracy of global GPP products in data-scarce mountain ecosystems of Southwest China. *Int. J. Appl. Earth Obs. Geoinf.* 144, 104908. <https://doi.org/10.1016/j.jag.2025.104908>.
- Warren, J.M., Pötzelberger, E., Wullschlegel, S.D., Thornton, P.E., Hasenauer, H., Norby, R.J., 2011. Ecohydrologic impact of reduced stomatal conductance in forests exposed to elevated CO₂. *Ecohydrology* 4 (2), 196–210. <https://doi.org/10.1002/eco.173>.
- Xia, L., Wang, F., Mu, X., Jin, K., Sun, W., Gao, P., Zhao, G., 2015. Water use efficiency of net primary production in global terrestrial ecosystems. *J. Earth Syst. Sci.* 124 (5), 921–931. <https://doi.org/10.1007/s12040-015-0587-4>.
- Xiao, J., Sun, G., Chen, J., Chen, H., Chen, S., Dong, G., Gao, S., Guo, H., Guo, J., Han, S., Kato, T., Li, Y., Lin, G., Lu, W., Ma, M., McNulty, S., Shao, C., Wang, X., Xie, X., Zhou, J., 2013. Carbon fluxes, evapotranspiration, and water use efficiency of terrestrial ecosystems in China. *Agric. For. Meteorol.* 182–183, 76–90. <https://doi.org/10.1016/j.agrformet.2013.08.007>.
- Xue, L., Fu, F., Chen, X., Liu, Y., Han, Q., Liao, S., Wei, Q., 2021. Analysis on water use efficiency of *Populus euphratica* forest ecosystem in arid area. *Theor. Appl. Climatol.* 145 (1), 717–730. <https://doi.org/10.1007/s00704-021-03636-7>.
- Yamazaki, D., Ikeshima, D., Tawatari, R., Yamaguchi, T., O'Loughlin, F., Neal, J.C., Sampson, C.C., Kanae, S., Bates, P.D., 2017. A high-accuracy map of global terrain elevations. *Geophys. Res. Lett.* 44 (11), 5844–5853. <https://doi.org/10.1002/2017GL072874>.
- Yang, Z.-L., Niu, G.-Y., Mitchell, K.E., Chen, F., Ek, M.B., Barlage, M., Longuevergne, L., Manning, K., Niyogi, D., Tewari, M., Xia, Y., 2011. The community Noah land surface model with multiparameterization options (Noah-MP): 2. Evaluation over global river basins. *J. Geophys. Res. Atmos.* 116 (D12). <https://doi.org/10.1029/2010JD015140>.
- Yuan, W., Cai, W., Liu, S., Dong, W., Chen, J., Arain, M.A., Blanken, P.D., Cescatti, A., Wohlfahrt, G., Georgiadis, T., Genesio, L., Gianelle, D., Grelle, A., Kiely, G., Knohl, A., Liu, D., Marek, M.V., Merbold, L., Montagnani, L., Xia, J., 2014. Vegetation-specific model parameters are not required for estimating gross primary production. *Ecol. Model.* 292, 1–10. <https://doi.org/10.1016/j.ecolmodel.2014.08.017>.
- Zhang, Q., Ficklin, D.L., Manzoni, S., Wang, L., Way, D., Phillips, R.P., Novick, K.A., 2019. Response of ecosystem intrinsic water use efficiency and gross primary productivity to rising vapor pressure deficit. *Environ. Res. Lett.* 14 (7), 074023. <https://doi.org/10.1088/1748-9326/ab2603>.
- Zhang, F., Ju, W., Shen, S., Wang, S., Yu, G., Han, S., 2014. How recent climate change influences water use efficiency in East Asia. *Theor. Appl. Climatol.* 116 (1), 359–370. <https://doi.org/10.1007/s00704-013-0949-2>.
- Zhang, W., Luo, G., Hamdi, R., Ma, X., Li, Y., Yuan, X., Li, C., Ling, Q., Hellwich, O., Termonia, P., De Maeyer, P., 2023. Can gross primary productivity products be effectively evaluated in regions with few observation data? *GISci. Remote Sens.* 60 (1), 2213489. <https://doi.org/10.1080/15481603.2023.2213489>.
- Zhang, T., Peng, J., Liang, W., Yang, Y., Liu, Y., 2016. Spatial-temporal patterns of water use efficiency and climate controls in China's Loess Plateau during 2000–2010. *Sci. Total Environ.* 565, 105–122. <https://doi.org/10.1016/j.scitotenv.2016.04.126>.
- Zhou, S., Yu, B., Huang, Y., Wang, G., 2014. The effect of vapor pressure deficit on water use efficiency at the subdaily time scale. *Geophys. Res. Lett.* 41 (14), 5005–5013. <https://doi.org/10.1002/2014GL060741>.
- Zhou, S., Yu, B., Huang, Y., Wang, G., 2015. Daily underlying water use efficiency for AmeriFlux sites. *J. Geophys. Res. Biogeosci.* 120 (5), 887–902. <https://doi.org/10.1002/2015JG002947>.
- Zscheischler, J., Mahecha, M.D., Avitabile, V., Calle, L., Carvalhais, N., Ciais, P., Gans, F., Gruber, N., Hartmann, J., Herold, M., Ichii, K., Jung, M., Landschützer, P., Laruelle, G.G., Lauerwald, R., Papale, D., Peylin, P., Poulter, B., Ray, D., Reichstein, M., 2017. Reviews and syntheses: An empirical spatiotemporal description of the global surface-atmosphere carbon fluxes: opportunities and data limitations. *Biogeosciences* 14 (15), 3685–3703. <https://doi.org/10.5194/bg-14-3685-2017>.